Sebastian Ruck
Herbert Oertel

Modelling the Bird Flight

Scientific Report 2007-2010

KIT Scientific Publishing

Sebastian Ruck, Herbert Oertel

Modelling the Bird Flight

Scientific Report 2007-2010

Modelling the Bird Flight

Scientific Report 2007-2010

by
Sebastian Ruck
Herbert Oertel

KIT Scientific Publishing

Author

Dr.-Ing. Sebastian Ruck
Prof. Prof. e.h. Dr.-Ing. habil. Herbert Oertel
Karlsruhe Institute of Technologie, Institute of Fluid Mechanics, Kaiserstr. 12, 76131 Karlsruhe

Impressum

Karlsruher Institut für Technologie (KIT)
KIT Scientific Publishing
Straße am Forum 2
D-76131 Karlsruhe
www.ksp.kit.edu

KIT – Universität des Landes Baden-Württemberg und nationales
Forschungszentrum in der Helmholtz-Gemeinschaft

KIT Scientific Publishing 2011
Print on Demand

ISBN 978-3-86644-761-5

Preface

The aerodynamics of flying birds and insects plays a crucial role in the domain of aeronautical engineering. The energy-efficient construction of winglets for airplanes, the formation flight of tactical aircraft or the drone engineering or military applications are inspired by birds. However, numerical and experimental studies of avian flight are limited. This holds also for flow and structure simulation of flapping wing motion, taking the unsteady aerodynamics and corresponding wing deformations into account at high flow velocities and flapping frequencies. The present scientific report gives an complete overview about the research on the aerodynamics of the avian flight at the Insitute of Fluid Mechanics, Karlsruhe Institute of Technology, Germany (Ruck and Oertel, 2010; Ruck and Tischmacher, 2010; Ruck et al. 2010a, 2010b; Oertel and Ruck, 2011).

Karlsruhe, September 2011 Sebastian Ruck and Herbert Oertel jr.

Contents

1 Introduction

In the last few decades, there have been growing successes in investigating the fluid dynamics of flying birds using various experimental techniques. Depending on the flow velocity (equal flight speeds) and the flapping frequency of the wingbeat, three idealized wake configurations have been established: 1. The discrete ring vortex gait (Rayner, 1979a, 1979b; Spedding, 1986) describes the wake configuration of slow flying birds by a series of separate vortex rings. The starting and stopping vortices of each downstroke are connected via the tip vortices and yield in separate elliptical or circular vortex rings, whereas the upstroke is aerodynamically inactive. The occurrence of the ring vortex structures in the wake was experimentally validated for numerous slow flying birds (Kokshaysky, 1979; Spedding et al., 1984; Spedding 1986, Spedding et al., 2003; Hedenström et al., 2006). 2. For increasing flow velocities the continuous vortex gait was observed (Rayner, 1986; Spedding, 1987). In this case, the upstroke acts more aerodynamically active leading to a decline of the spanwise shed starting and stopping vortices. The wake is increasingly dominated by tip vortices which follow the path of the wing tips. 3. A ladder wake is assumed for birds with an inflexible wing motion during acceleration at high and medium flight speeds (Pennycuick 1988; Hedrick et al., 2002). The wake is dominated by the tip vortices, which are connected by vortices of contrariwise circulation shed spanwise at the reversal points.
By means of wind tunnel tests using particle image velocimetry (PIV) the wake configurations of bats and birds for a wide range of flow conditions (Spedding et al., 2003; Hedenström et al., 2006; Hedenström, 2006; Hedenström et al., 2007; Hennigson et al., 2008; Rosén et al., 2004; Hubel et al., 2009) were investigated and various vortex models were developed. All observed wake configurations show ring vortex structures but differ from the idealized wakes. Double-ringed wakes consisting of ring vortices produced during the upstroke and downstroke were found for nightingales. The occurrence of root vortices at the wing base were observed for bats leading to complex vortex loops. Using simplified models of birds (Hubel and Tropea, 2005) and insects (Van Den Berg and Ellingtion, 1997a; 1997b) or flapping wings (Videler et al., 2004; Dickinsion and Götz, 1993; Poelma et al., 2006) the aerodynamics for low Reynolds number ranges or quasi stationary flow conditions were investigated experimentally. Numerical studies of bird aerodynamics at high reduced frequencies and Reynolds numbers are limited due to the modelling complexity and numerical validation of the applied methods.

The present scientific report gives an complete overview about the research on the aerodynamics of the avian flight at the Insitute of Fluid Mechanics, Karlsruhe Institute of Technology, Germany (Ruck and Oertel, 2010; Ruck and Tischmacher, 2010; Ruck et al., 2010a, 2010b; Oertel and Ruck, 2011). An three-dimensional avian flight model, the so called Kavian FM, was developed

to investigate the fluid mechanics of flapping flight for a wide range of flow velocities and wingbeat frequencies representing high Reynolds numbers and a high degree of unsteadiness to make a contribute to the ongoing research of avian flight. The results are obtained from interacting fluid-structure simulations and time resolved PIV measurements should help to understand the complex flow mechanism behind flapping wings.

1.1 Bird Feathers

A bird feather is composed of keratin and consists of the feather shaft and the feather vanes (Vexillum). The shaft can be divided into two regions: the Calamus (basal part) and the Rhachis (central part). The Calamus is a hollow tube and blends smoothly into the Rhachis which bears the vanes. The vanes consist of barbs (Rami), which are connected to one another with barbules (Radi) leading to a ripped surface structure of the vanes. The feather shaft consists of Medullar Foam which is surrounded by a Cortex.

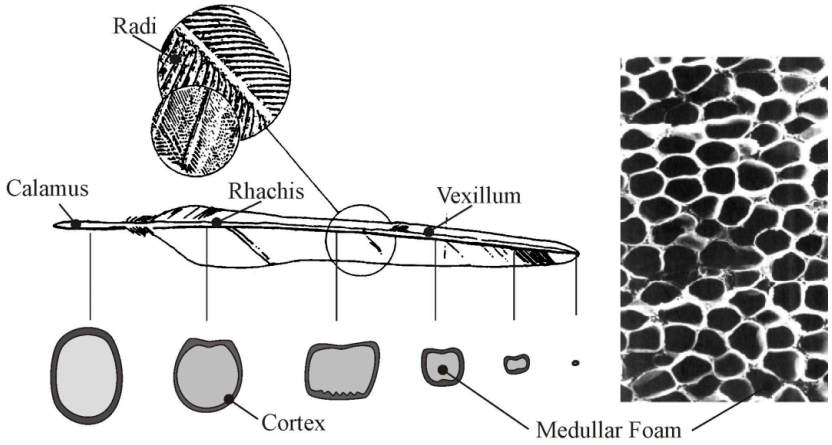

Figure 1: The composition of a bird's feather (Azuma, 2006; Oertel and Ruck, 2011).

The structural behaviour of a feather depends on the stiffness of the shaft, in particular the Cortex, and can be described by means of the corresponding Young's Modulus E. The Cortex is composed of β-Keratin molecules. The orientation of these molecules differs along the shaft influencing the corresponding Young's Modulus E. In direction of the shaft tip, the β-Keratin molecules are more and more longitudinal orientated leading to an increase of the Young's Modulus E. The mean Young's Modulus E of a primary feather is $\overline{E} = 2.5GPa$. Furthermore, the geometry of the shaft differs along the feather leading to changes in the second moment of area I for bending. Figure 2 shows the Young's Modulus E of a swanfeather (Bonser and Purslow, 1995) and the second moment of area I of a pigeon feather (Purslow and Vincent, 1978).

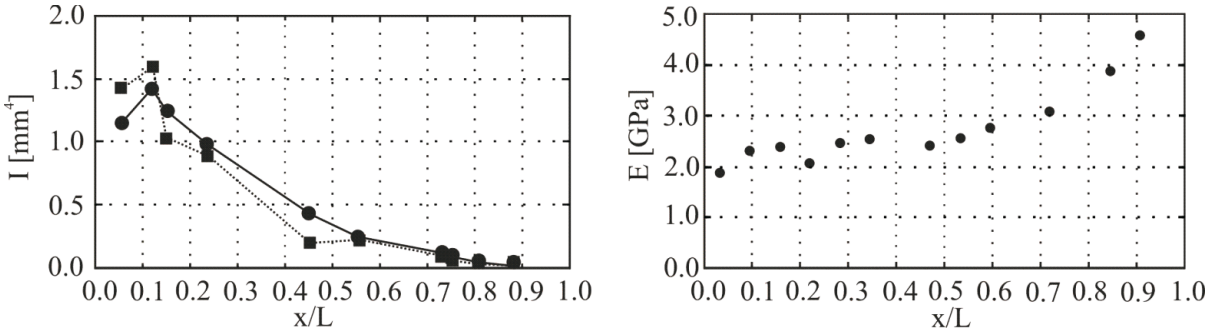

Figure 2: The second moment of area *I* of a pigeon feather (Purslow and Vincent, 1978) and the Young's Modulus *E* of a swan feather (Bonser and Purslow, 1995).

1.2 Aerodynamics of Flapping Flight

For increasing the lift and thrust generation, birds, bats and insects use different aerodynamic mechanism depending on the flow situation and wing kinematics during flapping flight. By means of experiments and numerical simulations using real animals and flapping models some effects were found out.

Dynamic Stall

Dynamic Stall or *Delayed Stall* occurs during a flapping wing motion with supercritical angles of attack. At the leading edge the so called *leading edge vortex* is generated which increases the circulation of the bound vortex resulting in a high pressure imbalance between the upper and lower wing side. The flow remains attached for longer on the wing and the stall is delayed. A secondary flow occurs parallel to the lateral wing axis and in direction of the wing tips. It stabilizes the leading edge vortex and limits the increase of the vortex by transporting vorticity to the tip vortices. The mechanism of *Dynamic Stall* was found for insects (Willmott et al., 1997; Van den Berg and Ellington, 1997b), birds (Videler et al., 2004; Ellington et al., 1996) and bats (Muijres et al., 2008).

Rotational Lift

The supination and pronation of the wing at the reversal points of the wingbeat cycle can increase the lift generation and is called *Rotational Lift*. Similar to the Magnus effect, the rotation of the wings causes an additional fluid transport close to the wing surface as a result of viscous forces. Depending on the upper or lower side of the wing and the relative flow velocities, the fluid close to the wing surface is accelerated on one side and decelerated on the opposite side. The occurring velocity differences lead to a pressure imbalance resulting in additional lift.

Wake Capture

During flapping flight vortex structures are generated in the wake. The flow separation of the bound vortices at the end of the upstroke and downstroke can cause vortex structures with different circulation. The interaction of the wings with the vortices in the wake can be used to a relative inflow in vertical direction proving additional momentum. Hovering insects use the *Wake Capture* to increase the lift and it is assumed that bird and bats use the mechanism of during slow flight and manoeuvring.

Clap and Fling

Using the C*lap and Fling* mechanism lift is provided immediately at the beginning of the downstroke. The clap is introduced by clapping the leading edges of both wings at the upper reversal points. By means of a rotation about an axis parallel to the lateral wing axis the clap is continued in direction of the trailing edge. The fling starts with opening of the clapped wings starting at the leading edge and wing tips. It is performed by rotating the wings about the trailing edge. By means of the fling, air is accelerated in the occurring gap between both wings leading to the development of bound vortices immediately at the beginning of the downstroke and thus lift is provided. Birds use the *Clap and Fling* mechanism for climbing and starting.

1.3 Wake Structures of Flapping Flight

The flow configurations and wake structures behind the flapping wings depend on the flow velocity (equals flight speed), flapping frequency, wing kinematics and wing design (Tobalske et al., 2003, Spedding et al., 2003, Oertel and Ruck, 2011). In the last few decades, there have been growing successes in investigating the wake structures of flying birds. Three idealized wake configurations have been established: the ring vortex gait, the continuous vortex gait and the ladder wake. Figure 3 shows the idealized vortex wakes.

Ring Vortex Gait

The discrete vortex ring gait (Rayner, 1979a, 1979b; Spedding, 1986) describes the wake configuration of slow flying birds by a series of separate vortex rings. At the beginning of each downstroke, a bound vortex is produced at the wing tips. Due to the well known vortex forming mechanism of classical airfoil theory (Oertel, 2009), corresponding contrariwise rotating vortices (starting vortex) are generated and shed to the wake. During the downstroke motion, the bound vortex is extended over the whole wing. The starting and stopping vortex of the downstroke is connected via the tip vortices which follows the path of the wing tips. At the end of the downstroke, the bound vortex is shed to the wake and yield in a separate elliptical or circular vortex ring. The upstroke is aerodynamically inactive and no vortex structures are generated by

the wing motion. The occurrence of the ring vortex structures was experimentally validated for numerous slow flying birds (Kokshaysky, 1979; Spedding et al., 1984; Spedding, 1986, Spedding et al., 2003; Hedenström et al., 2006).

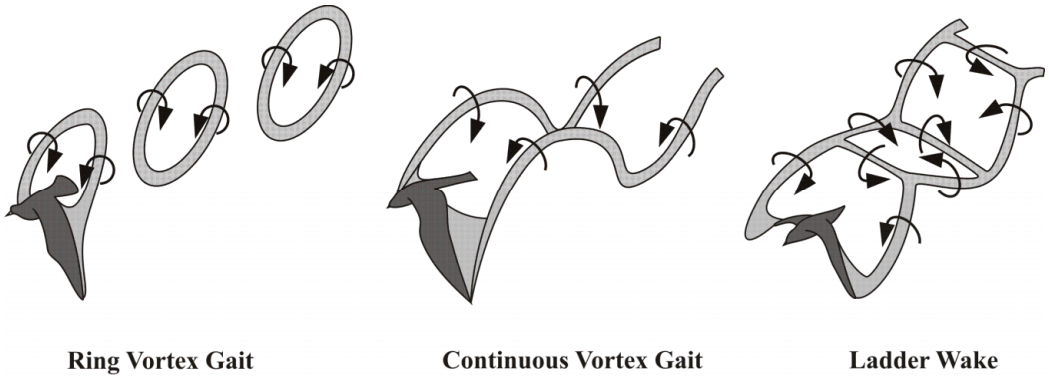

Figure 3.: Three idealized wake configurations: Ring Vortex Gait (Rayner, 1979b); Continuous Vortex Gait (Spedding, 1987); Ladder Wake (Pennycuick, 1988).

Continuous Vortex Gait

The downstroke and upstroke act aerodynamically active leading to the conservation of bound vortex circulation at the proximal wing area during the upstroke. Therefore, the spanwise shedding of starting and stopping vortices does not occur at the reversal points of the wingbeat cycle. The well pronounced tip vortices showing constant circulation direction follow the path of the wing tips and characterise the wake configuration. This type of wake configuration has been observed for bats (Rayner, 1986) and kestrels (Spedding, 1987).

Ladder Wake

During acceleration at high and medium flight speeds birds can use an inflexible wing motion which causes a ladder wake configuration (Pennycuick 1988; Hedrick et al., 2002,). At the reversal points of the wingbeat cycle, a spanwise shedding of starting and stopping vortices which were produced during upstroke and downstroke occurs. The vortex structures are connected via the tip vortices forming a ladder wake configuration.

Intermediary Wake

By means of wind tunnel tests using particle image velocimetry (PIV) measurement technique the wake configurations of bats and birds were investigated in detail. Various vortex structures were found showing ring vortex structures but differ from the idealized vortex wakes (Speeding et al., 2003; Hedenström et al., 2006; Hedenström, 2006). All wake configurations show ring vortex structures but differ from the idealized wakes. Double-ringed wakes consisting of ring vortices

produced during the upstroke and downstroke were found for nightingales and the occurrence of root vortices at the wing base were observed for bats leading to more complex vortex loops.

1.4 Wing Kinematics

During flapping flight birds use different kinematics for the lift and thrust production. The downstroke provides the bigger part of thrust and lift. The widespread wing moves downwards and rotates about the lateral wing axis (pronation) causing a forward pitching of the upper side of the wing. Wheras the downstroke kinematics are independent of the reduced frequency and invariant of morphological parameters, the upstroke kinematics differ enormously (Tobalske, 2000, 2007; Park et al., 2001; Oertel and Ruck, 2011). Birds with wings of low aspect ratio or/and round distal wings use the *flexed-wing* mechanism combined with a slightly *feathered* mechanism during the upstroke at all flight speeds. The proximal wing area is reduced by adducting the wrist and the distal wing area moves upwards and pitches backwards. The primary feathers are separated slightly. For birds with wings of high aspect ratio or/and pointed wings the upstroke kinematics depends on the flight speed. A *tip-reversal* mechanism is used at slow flight speeds, a *feathered* mechanism at intermediate flight speeds and a *swept-wing* mechanism at high flight speeds. During the tip-reversal mechanism, the wing area is reduced by adducting the wrist and a supination of the distal wing leads to a turning of the wing tip towards the flight direction. The upstroke occurs aerodynamically passive providing no thrust or lift and indicates the ring vortex gait. The swept-wing mechanism is characterized by a small supination of the wings and a slight adduction of the wrist. Therefore, the upstroke is aerodynamically active leading to a conservation of the bound vortex circulation during the upstroke and, thus, to the continuous vortex gait. The feathered mechanism combined with a slight tip-reversal at intermediate flight speed specifies the transition between the tip-reversal and the swept-wing mechanism.

2 FSI Simulation

2.1 Basic Equations

The physics of **fluid mechanics** are given by the conservation equations. For an incompressible fluid, the conservation equation for mass is:

$$\frac{\partial u_i}{\partial x_i} = 0 \tag{2.1}$$

and the conservation equation of momentum is:

$$\rho \cdot \left[\frac{\partial u_i}{\partial t} + u_j \cdot \frac{\partial u_i}{\partial x_j} \right] = h_i + \frac{\partial \sigma_{ij}^{\ F}}{\partial x_j} \tag{2.2}$$

with the flow velocity u_i, the density ρ, the volume force h_i and the stresses σ_{ij}^{F}. The stresses σ_{ij}^{F} can be subdivided into viscous stresses τ_{ij} and the pressure p:

$$\sigma_{ij}^{\ F} = \tau_{ij} - p \cdot \delta_{ij} \tag{2.3}$$

with the Kronecka Delta δ_{ij}.

By means of Stokes approach, Reynolds friction law can be used and the fluid based stress components can be expressed by velocity gradients:

$$\tau_{ij} = \mu \cdot \left(\frac{\partial u_i}{\partial x_j} + \frac{\partial u_j}{\partial x_i} \right) \tag{2.4}$$

with the the dynamic viscosity μ.

The conservation equations for mass and momentum are made dimensionless with the characteristic length l_{ch} representing the mean chord of a wing:

$$\vec{x}^* = \vec{x} / l_{ch},\ \vec{u}^* = \vec{u} / U,\ p^* = p/(\rho \cdot U^2),\ t^* = t \cdot f \cdot \pi \text{ and } \vec{h}^* = (\vec{h} \cdot l_{ch})/(\rho \cdot U^2) \qquad (2.5)$$

with the undisturbed flow velocity U.

Using the dimensionless characteristic Reynolds number $\mathrm{Re} = U \cdot l_{ch} \cdot \rho / \mu$ and the reduced frequency $k = f \cdot l_{ch} \cdot \pi / U$, we obtain the dimensionless equations:

$$\nabla \cdot \vec{u}^* = 0 \qquad (2.6)$$

$$k \cdot \left[\frac{\partial \vec{u}^*}{\partial t^*} + (\vec{u}^* \cdot \nabla)\vec{u}^* \right] = \vec{h}^* - \nabla p^* + \frac{1}{\mathrm{Re}} \cdot \Delta \cdot \vec{u}^* \qquad (2.7)$$

The equation of motion of the **structure mechanics** for the velocity of deformation v_i and the stresses σ_{ij}^S can be written:

$$\rho \cdot \frac{dv_i}{dt} = \rho \cdot \left(\frac{\partial v_i}{\partial t} + v_j \cdot \frac{\partial v_i}{\partial x_j} \right) = h_i + \frac{\partial \sigma_{ij}^S}{\partial x_j} \qquad (2.8)$$

The total time derivative of the rate of deformation describes the change in a volume element $dV = dx_1 \cdot dx_2 \cdot dx_3$ that is moving with the flow. This representation is called the Lagrange configuration. The partial time derivative of the rate of deformation with respect to time and the convective terms differentiated with respect to the space coordinates is called the Euler configuration.

2.2 Turbulence Modelling

The physics of flow are completely given by the conservation equations for mass (21) and momentum (2.2). The direct numerical solution (DNS) provides the full flow and turbulent spectrum and requires high temporal and spatial resolution. Regarding the enormous CPU cost, the usage of DNS is limited to simple flow problems or to low Reynolds to date. For the numerical simulations of bird flight, the Reynolds Averaged Navier Stokes (RANS) equations are used to solve the turbulent flow field. Using the Reynolds approach, any flow quantity ϕ can be subdivided into a time averaged quantity $\overline{\phi}(\vec{x})$ and its turbulent fluctuation $\phi'(\vec{x}, t)$:

$$\phi(\vec{x},t) = \overline{\phi}(\vec{x}) + \phi'(\vec{x},t) \qquad \text{with} \qquad \overline{\phi}(\vec{x}) = \frac{1}{\Delta t} \cdot \int_{t}^{t+\Delta t} \phi(\vec{x},t) \cdot dt \tag{2.8}$$

The conservation equations for mass and momentum of the time averaged continuity equation and the RANS equations given by:

$$\frac{\partial \overline{u}_i}{\partial x_i} = 0 \tag{2.9}$$

$$\rho \cdot \left[\frac{\partial \overline{u}_i}{\partial t} + \overline{u}_j \cdot \frac{\partial \overline{u}_i}{\partial x_j} \right] = \overline{h_i} - \frac{\partial \overline{p}}{\partial x_i} + \overline{\tau_{ij}} + \tau_{t,ij} \tag{2.10}$$

with the turbulent Reynolds-stresses $\tau_{t,ij}$, the time averaged flow velocity $\overline{u}_i$, the volume forces $\overline{u}_i$ and the viscous stresses $\overline{\tau}_i$.

Applying the Boussinesq approximation, the Reynolds stresses can be related to the mean velocity gradients:

$$\tau_{t,ij} = -\rho \cdot \overline{u_i' \cdot u_j'} = \mu_t \cdot \left[\frac{\partial \overline{u}_i}{\partial x_j} + \frac{\partial \overline{u}_j}{\partial x_i} \right] - \frac{2}{3} \cdot \rho \cdot k_t \cdot \delta_{ij} \tag{2.11}$$

with the velocity fluctuation u_i', the turbulent viscosity μ_t and the turbulent energy k_t.

By means to the two transport equations k-ω-SST model the turbulent viscosity is modelled (Menter 1993, 1994; Menter *et al.*, 2003). The k-ω-SST model combines the k-ε-model (Launder and Spalding, 1972) at the outer flow with the the k-ω-model of Wilcox (Wilcox, 1988) at near wall regions, transforming the k-ε-model to a k-ω-formulation. The original k-ω-equations are multiplied by the blending function F_1 and the transformed k-ε-model is multiplied by $(1-F_1)$. The blending function is $F_1=0$ at the outer flow and $F_1=1$ at the wall. The corresponding equations are added together and give the transport equations for the k-ω-SST model:

$$\rho \cdot \frac{\partial k_t}{\partial t} + \rho \cdot \overline{u}_i \cdot \frac{\partial k_t}{\partial x_i} = \widetilde{P}_k - \beta^* \cdot \rho \cdot \omega \cdot k_t + \frac{\partial}{\partial x_j} \left[(\mu + \sigma_k \cdot \mu_t) \cdot \frac{\partial k_t}{\partial x_j} \right] \tag{2.12}$$

$$\rho \cdot \frac{\partial \omega}{\partial t} + \rho \cdot \overline{u}_i \cdot \frac{\partial \omega}{\partial x_i} =$$

$$\alpha \cdot \rho \cdot S^2 - \beta \cdot \rho \cdot \omega^2 + \frac{\partial}{\partial x_j}\left[(\mu + \sigma_\omega \cdot \mu_t) \cdot \frac{\partial \omega}{\partial x_j} \right] + 2 \cdot \rho \cdot (1 - F_1) \cdot \sigma_{\omega 2} \cdot \frac{1}{\omega} \frac{\partial k_t}{\partial x_j} \frac{\partial \omega}{\partial x_j} \qquad (2.13)$$

The definition of the functions and model constants can be found in the literature (Menter et al., 2003; Fluent 6.3 User Guide, 2006). The accuracy of the k-ω-SST turbulence model is comparable to that of other 2-equation turbulence models. It is noted that small scale flow structures were filtered by the mesh size and a much finer grid connected to anisotropic turbulence models or DNS would be needed to resolve a wider or the complete flow and turbulence spectrum.

2.3 ALE Numerical Modelling

For flow-structure simulations, either a Lagrangian or an Eulerian configuration is applied to the computational domain. The conservation equations of structure mechanics are solved in the Lagrangian configuration with respect to a moving reference frame. For the solution of the corresponding flow field taking the grid motion into account an approach blending between the Lagrangian and Eulerian configuration is required. Therefore the equations for mass and momentum are given in the arbitrary Lagrangian-Euler formulation (ALE).

Considering the fundamental equations of structure mechanics (2.8) and fluid mechanics (2.1) (2.2) the can be added together: the rate of deformation v_i corresponds to the flow velocity vector u_i and the solid stresses σ_{ij}^S corresponds to the flow stresses σ_{ij}^F. Therefore, the equation (2.1), (2.2) and (2.8) can be added together leading to the ALE formulation for mass and momentum of an incompressible medium:

$$\nabla \cdot (\vec{v} - \vec{v}_G) = 0 \qquad (2.14)$$

$$\rho \cdot \left[\frac{\partial \vec{v}}{\partial t} + ((\vec{v} - \vec{v}_G) \cdot \nabla)\vec{v} \right] = \nabla \tilde{\sigma} + \vec{h} \qquad (2.15)$$

with the reference velocity $\vec{u}_G$ of the moving surface *G*. ρ denotes the density of the structure and of the fluid. The tensor $\tilde{\sigma}$ with the components is $\sigma_{ij} = \sigma_{ij}^S$ for the structure and $\sigma_{ij} = \sigma_{ij}^F$ for the fluid.

The ALE formulation enables the coupling of fluid mechanics and structure mechanics via the Lagrangian configuration on the moving surface *G*. By means of a partitioned code coupling, the fluid mechanics and structure mechanics are considered separately. The interaction is realized by a surface coupling approach providing the data exchange via the topologically identical surfaces *G* of both computational domains. The required coupling conditions for the data exchange can be formulated as follows:

Kinematic coupling condition - the velocity $\vec{v}$ and position $\vec{x}$ of the coupling surface *G* must be equal for fluid and structure:

$$x_i^F = x_i^S \qquad v_i^F = v_i^S \tag{2.16}$$

Dynamic coupling condition - the stresses acting on the coupling surface *G* and the corresponding local normalized vector $\vec{n}$ must be equal for fluid and structure:

$$\sigma_{ij}^F \cdot n = \sigma_{ij}^S \cdot n \tag{2.17}$$

Applying an explicit coupling scheme the numerical calculation of the structure equation and the flow equation are solved successively at each time step and the kinematic coupling quantites and the dynamic coupling quantities are exchanged at the interface *G*. Regarding the structural stiffness and the ratio of fluid density to structural density, 'added-mass' effects causing instabilities (Oertel and Ruck, 2011) can be neglected for aeroelastic problems.

2.4 Software

The numerical flow simulations were performed by the finite volume method in the ALE formulation as implemented in the FLUENT solver (ANSYS Germany GmbH, Darmstadt, Germany). By means of the Reynolds averaged Navier-Stokes (RANS) approach (Oertel and Ruck, 2011), turbulence viscocity was modelled by the shear-stress transport (SST) k-ω model (Menter, 1993; Menter et. al 2003). For the spatial and time discretization, standardized approximation schemes were applied (2nd Order Upwind and Euler implicit schemes, respectively). The algebraic equation system was solved using the SIMPLE algorithm. The numercial structure simulation was conducted by the finite element solver ABAQUS (SIMULIA Inc., Providence, USA). The nonlinear dynamic equilibrium equations were solved at each time increment applying implicit integration schemes. For coupling the FLUENT and ABAQUS

solver providing flow-structure interaction the coupling library MpCCI (Mesh based parallel Code Coupling Interface, Fraunhofer Institute, Sankt Augustin, Germany) was used and an explicit serial coupling scheme was applied. Node positions and relative wall forces were exchanged at the coupling surface *G* for each time step.

3 Methods and Models

3.1 Kavian Flight Model

A three-dimensional model was developed to investigate the flapping flight of birds in a simplified manner for a wide range of flow velocities and wingbeat frequencies. The model consists of two elastic wings, a rigid body, a flapping gear mechanism, a mounting suspension and a drive unit. The model was abstracted from birds, but does not represent real geometry. The modelling was influenced by restrictions in manufacturing for the mechanical realisation and by the specifications of grid generation for fluid structure simulations. The wing consists of an adapter and a membrane. The adapter forms the round leading edge and has a rectangular support for the elastic membrane on the opposite. It transfers a predefined motion to the front side of the elastic membrane facilitating the flapping motion. Except the front side of the wing, the membrane acts passively and its movement depends on the initial and aerodynamic forces. A stiff frame was added to the adapter and membrane sideways at the wing base for stabilization. The wing span is *0.543 m*, the wing area is *313.8 cm*^{2} and the mean chord is *0.08 m.* To realize the flapping motion without geometrical interferences, the wings were placed sideways the body, creating a small gaps. The rigid body was amended by semicircular protrusions to prevent flow through these gaps. The corresponding geometry data of the avian flight model shown in Fig. 4 and the corresponding material data of the wing components are set out in Table 1.

Component	Material	*E [GPa]*	ρ *[kg/m^3]*	ν
Adapter	Aluminium	70	2700	~ 0.43
Membrane	Polyurethane	2	1190	~ 0.49
Frame	Aluminium	70	2700	~ 0.43
Body enclosure	Carbon fiber-reinforced polymer			
Gear	Steel			

Table 1: Materials of the model components.

In the real wingbeat kinematics of birds and bats (Rosén *et al.*, 2004; Tian *et al.* 2006), the flapping motion can be approximated as a periodic function. For simplification, the flapping motion was abstracted by a wing rotation about a single hinge (Azuma, 2006). Neglecting the forward velocity of the wing relative to the body, the wing motion was simplified by a periodic

function using two degrees of freedom: A sinusoidal rotation about the off-centre axis parallel to the body axis provides the flapping motion and the pitching of the wing was realised by a phase-delayed rotation about the moving lateral wing axis. The maximum and minimum flapping angles were $\gamma_{min/max} = \pm 30\,°$ and the corresponding angles of attack were $\theta_{min/max} = \pm 20\,°$.

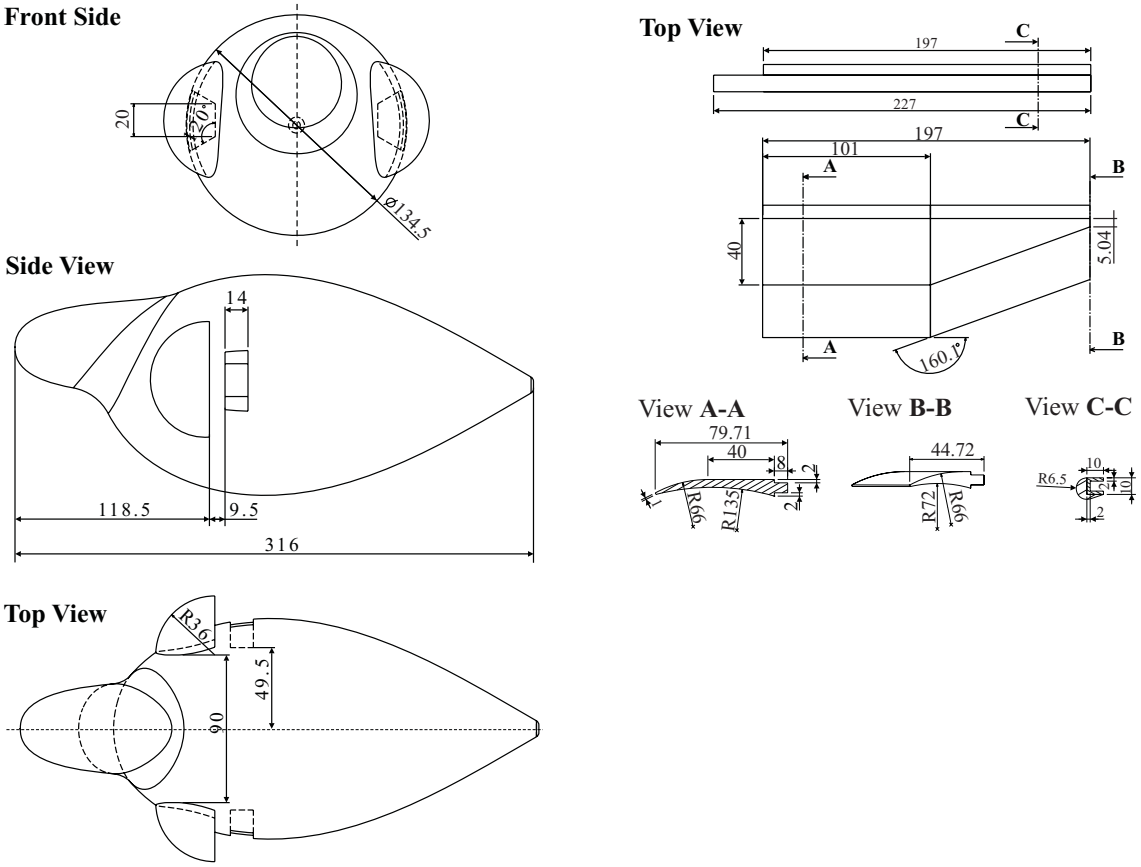

Figure 4: Geometrical properties of the Kavian Flight Model.

3.2 Geometrical and Kinematical Model

A mechanical representation of the Kavian FM was developed to facilitate experimental investigations in the wind tunnel. The model was constructed and built at the Institute of Fluid Mechanics, Karlsruhe Institute of Technology.

The simplified flapping motion of the model was realized by the sinusoidal rotation about two axes for the flapping and pitching of the wing. Therefore, a flapping gear mechanism was developed proving a simultaneous, phase-delayed sinusoidal rotation about two axes. a cardan joint transforming mechanical strokes into rotations was used for the flapping gear mechanism which was placed inside the body. Fig. 5 shows the flapping gear of the Kavian FM. The cardan gear, the mounting suspension and the drive unit were built of iron steal. By means of two

connection rods the required stroke was supplied. Both rods were connected to the crank of the drive unit. The crank was powered by a servodrive (AMC Europe) which was controlled digital by a computer via a RS2322 interface. The material depending maximum flapping frequency was f = 15 Hz with a safety coefficient of about S = 1.7.

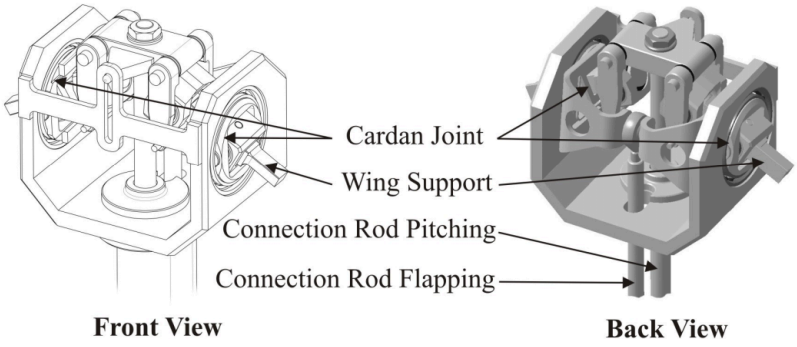

Figure 5: Flapping gear of the Kavian FM.

3.3 Numerical Models

To simulated flow-structure interaction with the applied partitioned coupling approach the generation of two numerical models with topologically identical surfaces is required: a structure model and a flow model.

The structural model consists of the wings including the membrane, the adapter and the stiff frame. The corresponding mechanical properties are shown in Table 1. By means of tetra cells the grid generation was performed automatically and a good quality mesh (cell average shape factor *ASF=0.7*) was generated. The components were modelled as homogeneous materials with isotropic material behaviour, constant densities ρ_m and linear Young's modulus E. For all simulations, the mechanical properties of the adapter, frame and membrane are consistent. The wingbeat motion was implemented by applying the predefined periodic functions to the stiff adapter transferring the wing kinematics. The flow model represents the fluid domain and contains the wings, the body and the mounting suspension. By means of automatic grid generation, an unstructured mesh of tetra cells was built with refinements close to the model. Because of the moving and deforming wing surface, the grid needed to be remeshed at each calculation time-step. The remeshing and smoothing algorithms for the dynamic mesh generation were provided by the FLUENT solver. Both models are shown in Fig.6.

A grid sensitivity study for the flow simulations was performed. Different grids were created additionally by coarsening the simulation grid close to the model and in the wake retaining the identical geometry setup. The generation algorithm was the same in all three grids. The Grid

Convergence Index (GCI) method (Roach, 1998) was applied for determining the numerical uncertainty for three grids with cell numbers of 1,524,000, 792,000 and 466,000 close to the model and in the wake corresponding to total cell numbers of 1,780,000, 1,020,000 and 720,000.

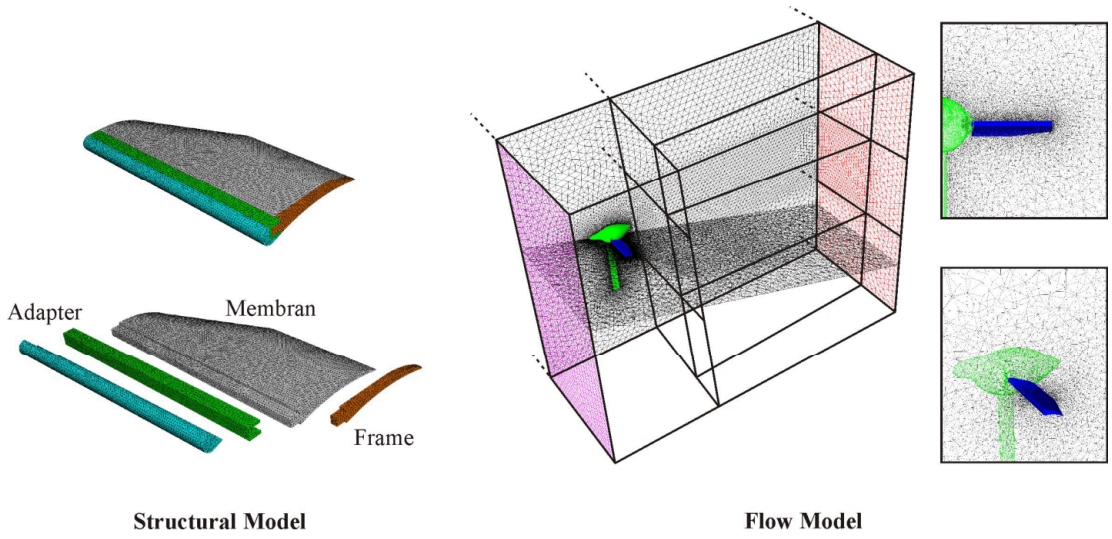

Figure 6: Numerical representation of the Kavian FM.

Fig 7 shows the amplitudes of the velocity magnitudes $|u_{Amp}|$ and its extrapolated values with the discritization error bars at three different points in the wake for the different meshes at a reduced frequency of $k = 0.67$ and $k = 0.22$. Point p_1, p_2 and p_3 were placed downstream at intervals of $d_1 = 0.3\ m$, $d_2 = 0.6\ m$, $d_2 = 0.9\ m$ at mid wing position.

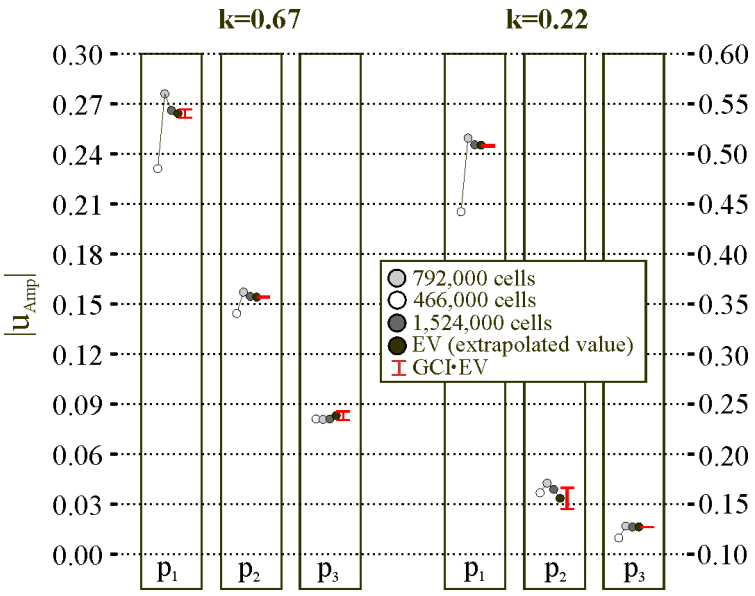

Figure 7: Velocity amplitudes with the corresponding extrapolated values and GCI at points p_1, p_2 and p_3 in the wake for k=0.67 and k=0.22.

As it can be seen, the extrapolated values for the velocity amplitudes of the simulation grids show convergence and the results of the finest grid are close to the extrapolated values and fit the error bar limit. The maximum fine-grid convergence index of 0.067 was determined at point p_2 for $k = 0.22$ which corresponds to an extrapolated error of $a^{ext} = 5.8\%$.

3.4 Wind Tunnel Experiments

The experiments were performed in the closed-circuit, low turbulence (turbulence intensity $t_I <$ 1%) wind tunnel at the Institute for Hydromechanics, Karlsruhe Institute of Technology, Germany. By means of time resolved particle image velocimetry (TR-PIV) technique the transient velocity distributions perpendicular to the flow stream were measured in 2-dimensional planes behind the avian flight model. The large working section of the wind tunnel offers a wide area for flow measurements in the wake. For the experiments the mechanical model was placed in front of the wind tunnel nozzle centre. The velocity measurements were carried out by means of a Dantec Dynamics 2D-2C TR-PIV System. Therefore the air in the wind tunnel was seeded with small tracer particles (particle size d_p =1-3 μm). Using a Nd:YAG laser (14 mJ/pulse at a recording frequency of 1kHz, wavelength λ = 532 nm), plane light sheets were generated to illuminate parts of the measuring areas. A high-speed CMOS camera (SpeedSense 9072, 1280x800 pixels) was placed sideways to capture the particle displacement of the seeded air. Four different measuring areas were located behind the midwing position and behind the body of the avian fight model, see Table 2 and Fig. 8 for details. The averaged spatial resolution of the areas was R = $0.173 \cdot 10^{-3}$ m/pixel. To obtain the temporal relation between the velocity fields recorded at the different measuring areas, a LED signal which indicates the upper wing position was captured with the high-speed camera illuminating a small image section (3 x 3 pixels) at the top right margin of an image.

Distance	Plane A	Plane B
d_1	55 mm	55 mm
d_2	157 mm	195 mm
d_3	0 mm	175 mm
d_4	188 mm	197 mm
d_5	105 mm	105 mm

Table 2: Geometrical parameters of the measuring areas.

Applying a double-frame/single exposure mode (Raffel et al., 2007), the wake configuration was measured for two reduced frequencies, $k = 0.22$ and $k = 0.67$. The interrogation areas (*IA*) were 32 x 32 pixels without overlap, corresponding to area size of $5.5 \cdot 10^{-3}$ m x

$5.5 \cdot 10^{-3}$ m. The velocity vectors were calculated by means of an adaptive correlation (Dantec Dynamics). In consideration of the spatial resolution and mean flow velocities, the minimum TR-PIV measuring frequency $f_{M,min}$ for the experiments was determined. It was assumed, that the smallest vortex structure can be captured by a field of 3 x 3 *IA*. It corresponds to a length of $3 \cdot IA = 16.62 \cdot 10^{-3}$ m in main flow direction which can be covered maximal by a vortex structure at the flow velocity U between the time span Δt,

$$U \cdot \Delta t = \frac{U}{f_c} = 3 \cdot IA \tag{3.1}$$

where f_c is the critical measuring frequency. Taking the Nyquist-theorem (Hoffmann, 2005) into account, the minimum TR-PIV measuring frequency $f_{M,min} > 2 \cdot f_c$ for a distortion-free reconstruction of the flow structures can be determined, leading to a measurement frequency of $f_M(k=0.67) = 500\ Hz$ and of $f_M(k=0.22) = 1040\ Hz$ (maximum camera frequency). The corresponding interframe time between two light pulses was $t_i(500\ Hz) = 400\ \mu s$ and $t_i(1040\ Hz) = 170\ \mu m$.

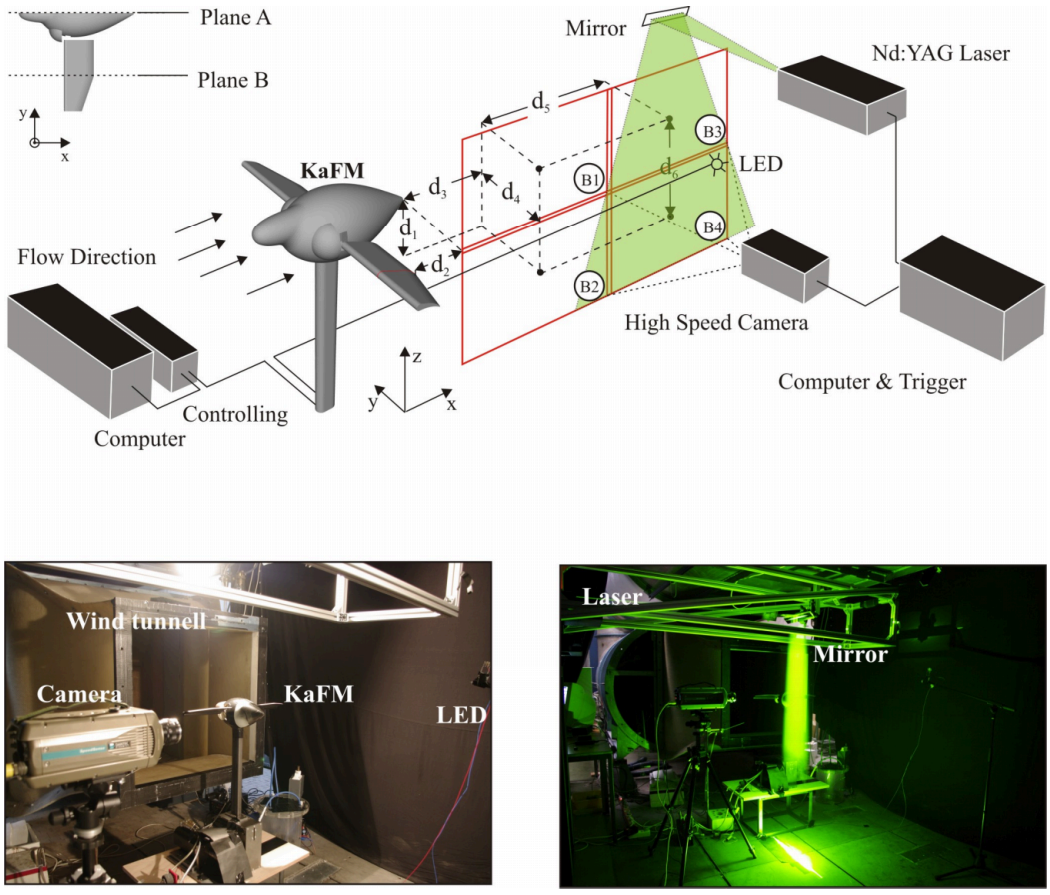

Figure 8: Experimental setup of the TR-PIV measurements.

4 Results

4.1 Performance

The flow conditions used in the experiments and simulations correlate with those determined for birds (Spedding et al., 2003; Rosén et al., 2004; Tobalske and Dial, 1996) and bats (Hedenström et al., 2007; Tian et al., 2006). The corresponding reduced frequencies range from $k_{min}=0.22$ to $k_{max}=1.00$.

FSI Simualtions

The FSI simulations were performed for three different flow velocities, $U=3, 6, 9\ ms^{-1}$ and three wingbeat frequency of $f=8, 10, 12\ Hz$. Aerodynamic quantities and mechanical quantities were recorded at a write frequency of $f_w=200\ Hz$ (for $f=8, 10\ Hz$) and $f_w=330\ Hz$ (for $f=12\ Hz$). Lift and drag forces were recorded at a frequency of $f_w=1\ kHz$. For the post-processing one steady state wingbeat cycle was considered providing data of a fully developed flow field. Hence, *21(10 Hz)*, *26(8 Hz)* and *29(12 Hz)* solved data sets were obtained.

Experiments

The experiments were performed for two different flow velocities, $U=3, 9\ ms^{-1}$ and a constant wingbeat frequency of f=8 Hz. The measurement frequency was $f_M(k=0.67) = 500\ Hz$ and of $f_M(k=0.22) = 1040\ Hz$. For analyzing the wingbeat induced wake flow, the recorded velocity fields of the measuring areas were phase-averaged taking the intermittency of the wake flow into account. Therefore, additional vortex structures occurring non-periodically were filtered. By means of the recorded LED signal which indicates the upper wing position, the results of the experiments and the numerical simulations were related to each other.

4.2 Validation

Physical parameters and quantities

The physical parameters and quantities of measuring area B3 and B4 resulting from the TR-PIV experiments and the FSI simulations at a reduced frequency of $k = 0.67$ ($f=8\ Hz, U=3\ ms^{-1}$) and $k = 0.22$ ($f=8\ Hz, U=8\ ms^{-1}$) are set out in Table 3.

The flapping frequency f and flow velocity U differ marginal and yield to comparable Reynolds numbers Re and reduced frequencies k. The time averaged velocities u_x, u_y, u_{mag} are the spatial

mean velocity of one measuring area phase-averaged over 40 wingbeat cycles. The time averaged fluid velocities obtained by the experiments and numerical simulations are in good agreement for u_x and u_{mag} and differ for u_y. The experimental results show higher fluid velocities perpendicular to the main flow direction. It is assumed, that the applied numerical approach underestimates the wing motion induced flow in the wake as a result of coarse spatial resolution filtering small velocity fluctuations and leads to smooth velocity profiles. The high resolved experiments enable the capturing of these small velocity fluctuations. Furthermore, the symmetry condition of the numerical flow model inhibits vortex shedding from the model body which can occur during the experiments. The wind tunnel geometry and the measurement setup are not provided for the numerical simulation.

k = 0.67		Measuring Area 3B		Measuring Area 3B	
		FSI	TR-PIV	FSI	TR-PIV
Flapping frequency f	Hz	8.00	7.90	8.00	7.90
Flow velocity U	ms^{-1}	3.00	2.89 ± 4%	3.00	2.89 ± 4%
Time-averaged x-velocity u_x	ms^{-1}	3.26	3.26	3.36	3.42
Time-averaged y-velocity u_y	ms^{-1}	0.14	0.26	-0.17	-0.24
Time-averaged velocity magnitude u_{mag}	ms^{-1}	3.31	3.35	3.42	3.53
Reynolds number Re	-	16400	15800	16400	15800
Reduced frequency k	-	0.67	0.69	0.67	0.69
k = 0.22		Measuring Area 4B		Measuring Area 4B	
		FSI	TR-PIV	FSI	TR-PIV
Flapping frequency f	Hz	8.00	7.88	8.00	7.88
Flow velocity U	ms^{-1}	9.00	9.00 ± 4%	9.00	9.00 ± 4%
Time-averaged x-velocity u_x	ms^{-1}	9.00	8.93	8.88	8.67
Time-averaged y-velocity u_y	ms^{-1}	-0.16	-0.25	-0.14	-0.30
Time-averaged velocity magnitude u_{mag}	ms^{-1}	8.91	8.97	8.70	8.89
Reynolds number Re	-	49300	49300	49300	49300
Reduced frequency k	-	0.22	0.22	0.22	0.22

Table 3: Physical parameters and quantities.

For a quantitative validation of the numerical approach, the velocity profiles determined at the centre point of the measuring areas were analyzed at a reduced frequency of $k = 0.67$ *(f=8 Hz, U=3* ms^{-1}*)* and $k = 0.22$ *(f=8 Hz, U=8* ms^{-1}*)*. Fig. 9 shows the temporal development of the magnitude flow velocity u_{mag} measured at the measuring area 3B and 4B. The results of the experiments are phase-averaged over 40 wingbeat cycles filtering non-periodically vortex structures and given with its *95%* confidence intervals. The corresponding amplitude spectrums are set out in Fig. 10.

The wingbeat motion indicates low-frequent vortex shedding which leads to continuously alternating flow velocities throughout the wingbeat. The velocities displayed in Fig. 9 can be characterized by the minima and maxima. The temporal development of the minima and maxima velocities determined experimentally and numerically are in good agreement for $k = 0.67$, whereas the temporal development differs slightly for $k = 0.22$. For both reduced frequencies the difference between the instantaneous velocity of the experiments and simulations is $< 10\%$; the maximum was 9.2% for $k = 0.67$. The experimental results show high-frequent fluctuations of the velocities which were not found for the numerical results. It can be explained by a continuously shedding of small scale vortex structures occurring at the wings, body and model suspension which were captured additionally by the high resolved experiments, whereas the coarser spatial resolution of the numerical approach damps those structures leading to a smooth velocity development.

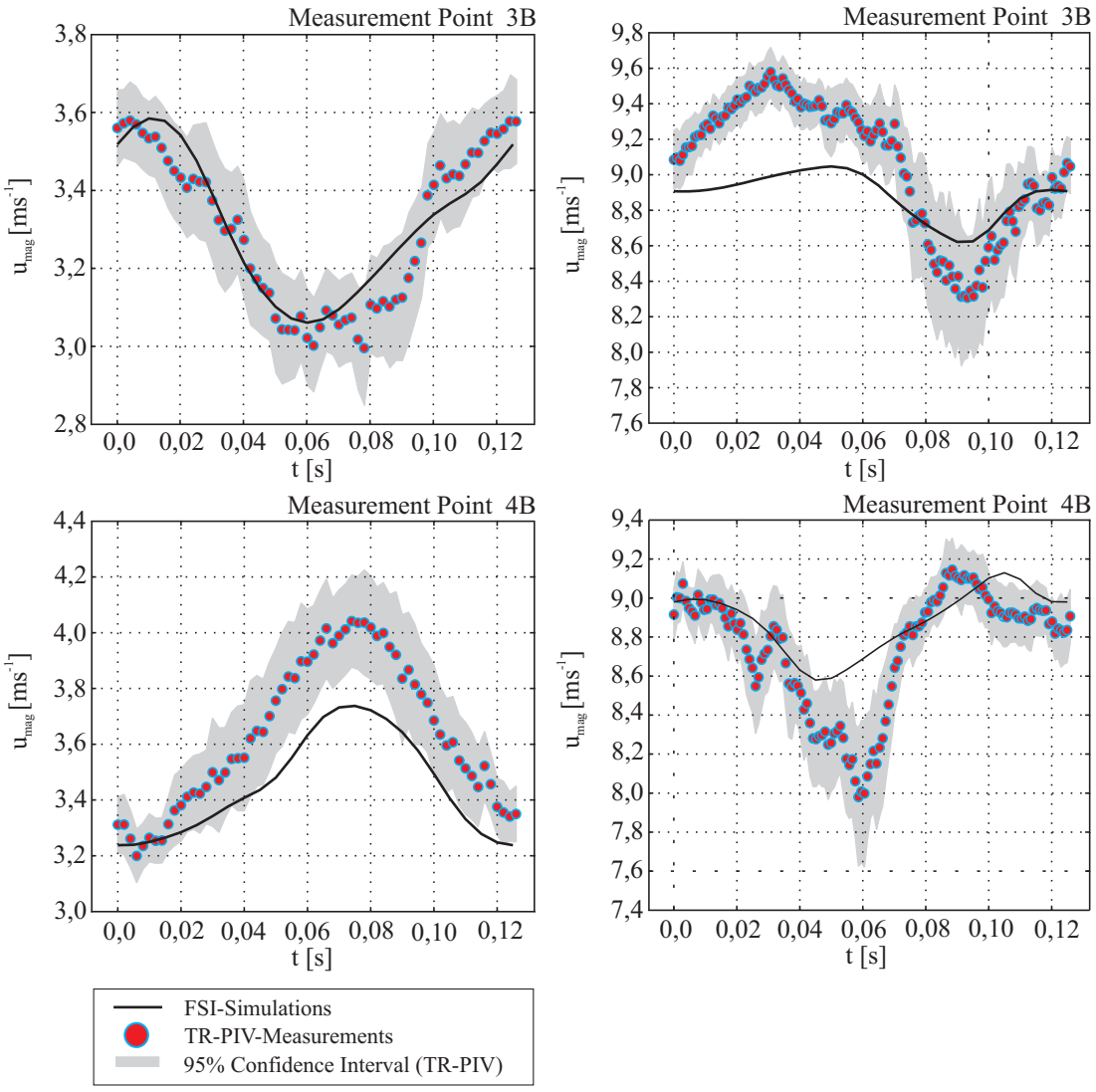

Fig 9: Magnitude flow velocity u_{mag} measured at the centre points of measuring area 3B and 4B.

The high frequent fluctuations affect the corresponding amplitude spectrums shown in Fig. 10. The fundamental frequency which is based on the wingbeat motion causing the shedding of counter rotating vortices is $f = 8\ Hz$ for the numerical simulations and $f = 7.9\ Hz$ for the experiments. The harmonics of the fundamental frequency decrease for increasing frequencies. For a reduced frequency of $k = 0.22$ the harmonic amplitude increases at a frequency of $f = 40\ Hz$ before continue to decrease. It is assumed, that the fifth harmonic and periodical vortex shedding interfered with each leading to an accumulation of the amplitudes. For $f > 100$ no further amplitudes were found.

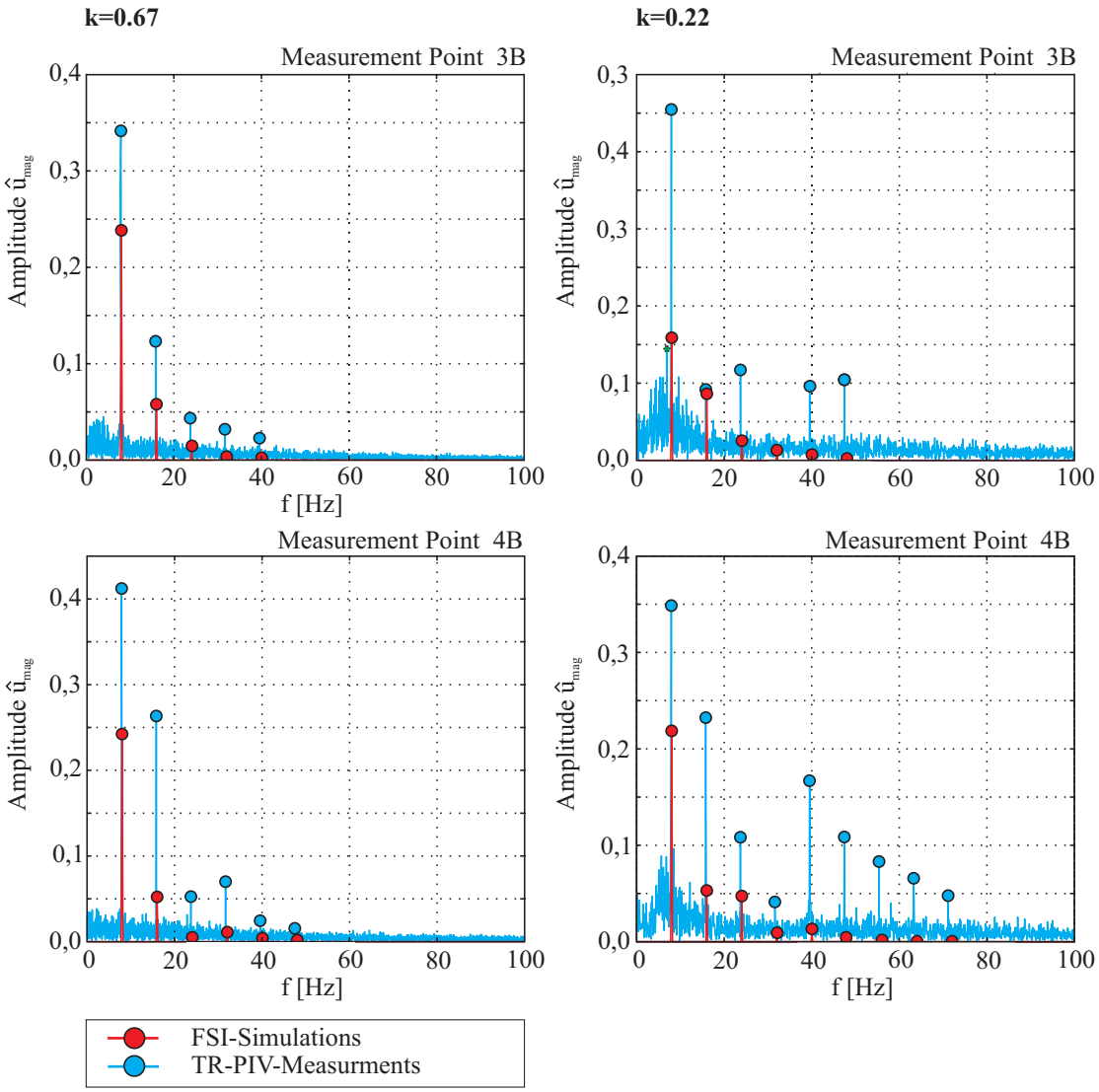

Figure 10: Amplitude spectrum of the Magnitude flow velocity u_{mag}.

Qualitative Analysis

For a qualitative validation of the FSI simulations, two-dimensional streamline plots determined at the measuring areas were analyzed at a reduced frequency of $k = 0.67$ ($f=8$ Hz, $U=3$ ms^{-1}) and $k = 0.22$ ($f=8$ Hz, $U=8$ ms^{-1}). Taking the intermittency into account, the results of the experiments are phase-averaged over 40 wingbeat cycles. For the generation of the streamline plots the velocity component u_x in flow direction minus the instantaneous, spatial-averaged velocity of the measuring area was used. The measuring areas overlap with each other providing a relation of the different flow structures.

Fig. 11 – Fig. 14 show the streamline plots determined at the measuring area 3B and 4B for the time steps $t/t_0 = 0.00$, $t/t_0 = 0.28$, $t/t_0 = 0.52$ and $t/t_0 = 0.76s$. Based on the LED signal, the deviation between the experiments and the simulations were $\pm 2 \cdot f_R = 0.004$ s and ± 0.0144 m for $k = 0.67$ and $\pm 5 \cdot f_R = 0.0048$ s and ± 0.036 m for $k = 0.22$. The streamline plots are dominated by focus F, saddle points S and nodal points K indicating different vortex structures (Oertel, 2009). As with the results of the quantitative analysis, the macroscopic vortex structures of the TR-PIV experiments and the FSI simulations are in a good agreement for a reduced frequency of $k = 0.67$, whereas the additional occurrence of small scale flow structures lead to differences of the two-dimensional streamline plots for a reduced frequency of $k = 0.22$.

For a reduced frequency of $k = 0.67$ the flow field of measuring area 3B is dominated by the focus F_1 which moves upwards in main flow direction at $t/t_0 = 0.00$. The results of the TR-PIV measurements show an additional vortex structure indicated by focus F_2. At the measuring area 4B focus F2 is continued and was found for the experiments and simulations. It is assumed, that the vertical stretching of the flow structures is caused by the differences in the velocity components u_y. The nodal point K1 is also given at $t/t_0 = 0.00$. The movement of focus F_3 and the corresponding saddle point S_3 can be seen at $t/t_0 = 0.28$, $t/t_0 = 0.52$ and $t/t_0 = 0.76$ for both measuring areas. At $t/t_0 = 0.76$ the counter rotating focus F_4 occurs on the left. Because of the additional vortex shedding at higher flow velocities the streamline plots differ for a reduced frequency of $k = 0.22$. Considering the streamline plots, it can be seen, that the relation of flow structures between the measuring areas is more complicated. At $t/t_0 = 0.00$, $t/t_0 = 0.52$ and $t/t_0 = 0.76$ the streamlines plots of the experiments are comparable to those of the numerical simulations for both measuring areas. The results show no vortex structures at $t/t_0 = 0.00$ and the flow fields are dominated by vortices at the following time steps. At $t/t_0 = 0.28$ the flow structures determined experimentally and numerically differ. Whereas the numerical results show unidentified flow structures, the flow field of the TR-PIV measurements is dominated by focus and saddle points. Furthermore, the streamline plots of the experiments are not as smooth as those of the simulations.

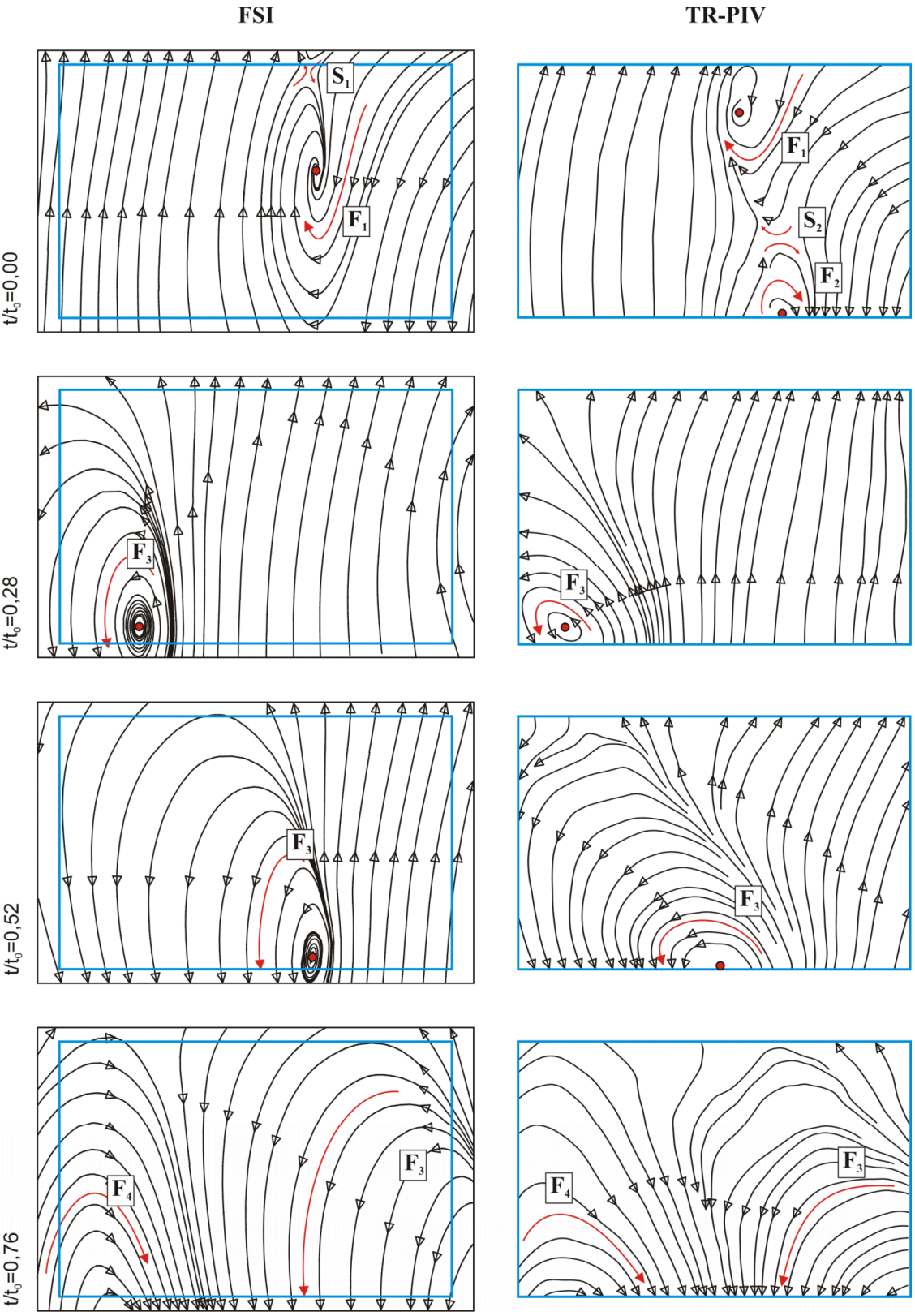

Figure 11: Streamline plots of measuring area 3B at *k = 0.67*.

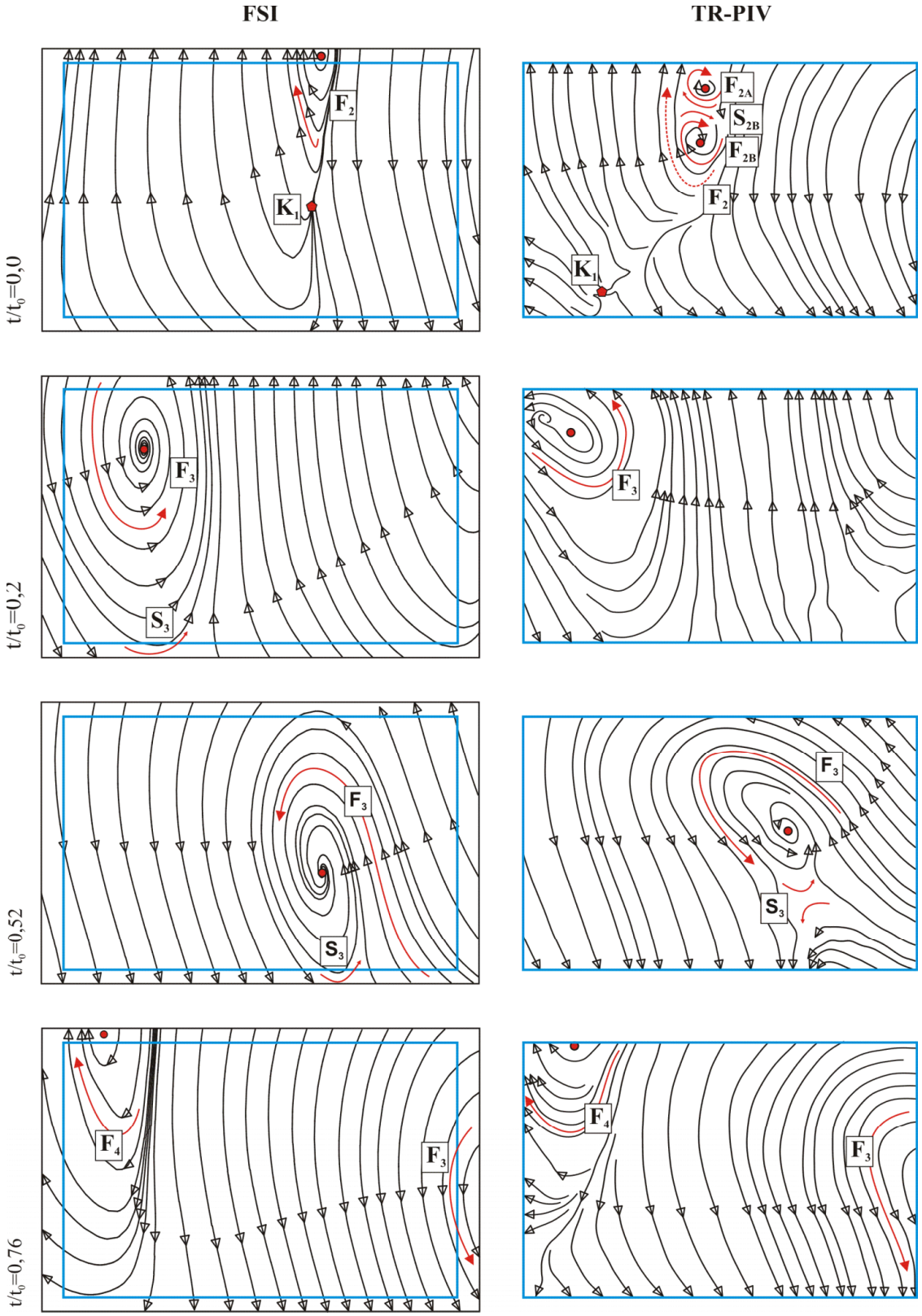

Figure 12: Streamline plots of measuring area 4B at $k = 0.67$.

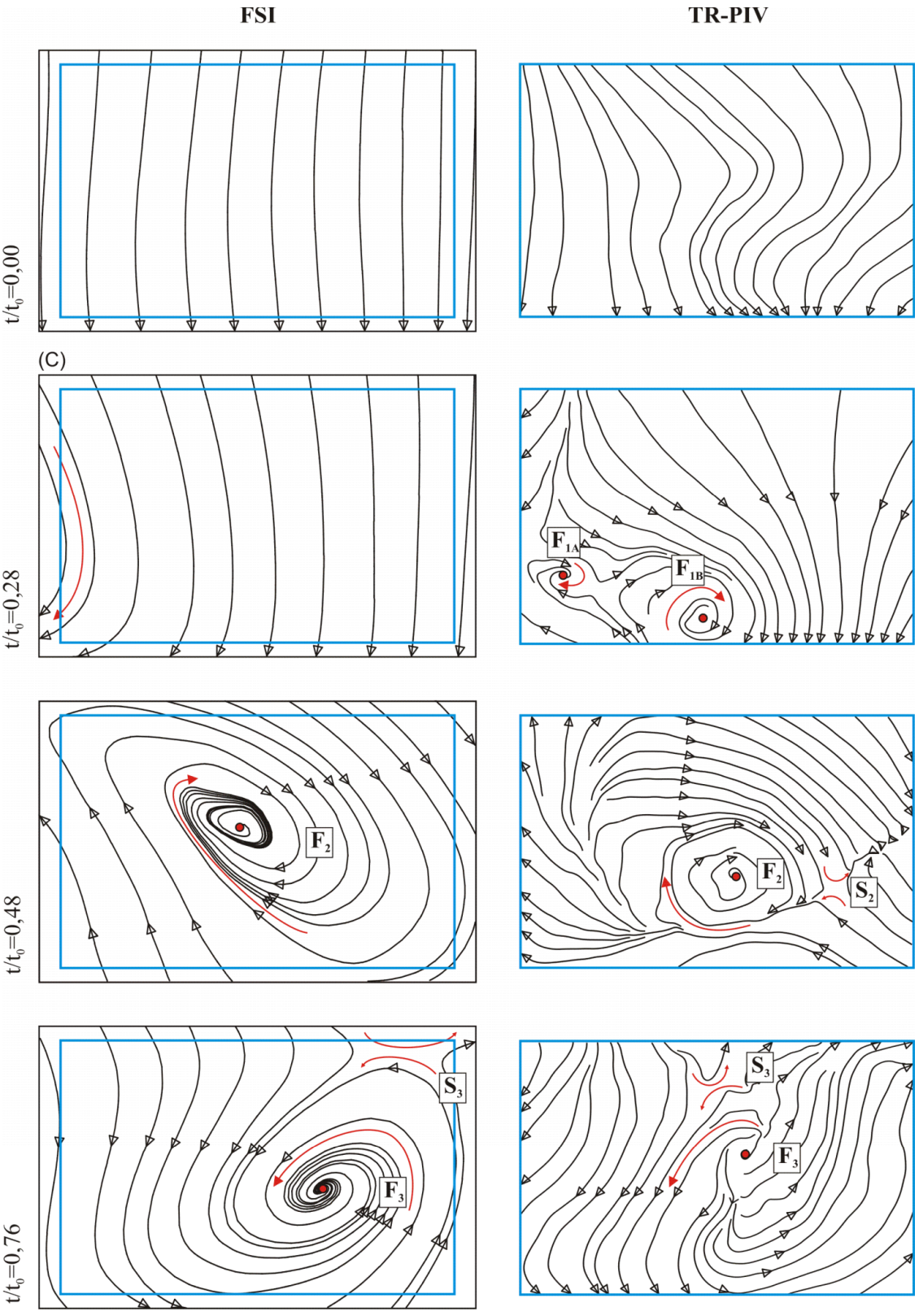

Figure 13: Streamline plots of measuring area 3B at *k = 0.22*.

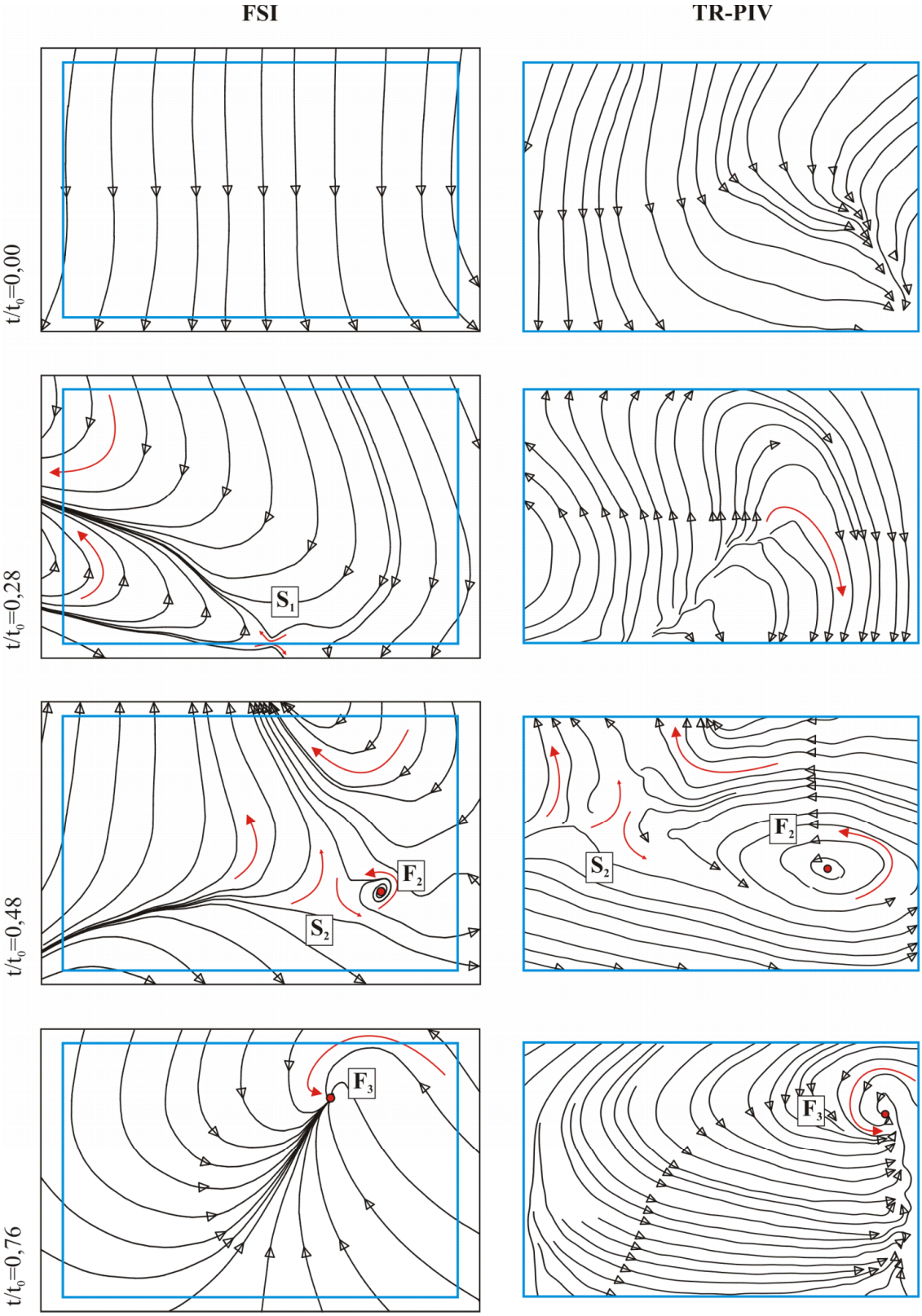

Figure 14: Streamline plots of measuring area 4B at $k = 0.22$.

4.3 Wake Configuration

To understand the complex wake flow and to reconstruct the vortex configuration, flow structures were visualized by displaying regions of pressure minima using isosufaces of the λ_2 method (Jeong and Hussain, 1993). Three different flow conditions representing the high reduced frequency range, the intermediate reduced frequency range and low reduced frequency range were analyzed in detail. Fig. 15 - Fig.23 show the flow structures at the time steps $t/t_0 = 0.00$, $t/t_0 = 0.28$, $t/t_0 = 0.52$ and $t/t_0 = 0.76$ and a corresponding schematic description.

k=0.67 (f=8 Hz, U=3 ms^{-1})

At high reduced frequencies (*k=0.67, f=8 Hz, U=3 ms^{-1}*), the wake is dominated by series of separated vortices behind each wing. The wake pattern consist of different ring vortex structures. The starting and stopping vortices shed at the reversal points of the upstroke and downstroke interlock with each other and form a continuous wake. At the beginning of the downstroke, a clockwise rotating bound vortex is produced around the wings. The corresponding anticlockwise rotating vortices (starting vortex) are shed to the wake. At the upper reversal point of the wingbeat cycle the separation of the starting vortex begins by the generation of a vortex sheet which extends widely over the wing. The vortex sheet contains the starting vortex structure and clockwise and anticlockwise rotating small scale vortices which are shed continuously into the wake. The separation starts at the wing tip and shifts to the wing base while moving downwards. The bound and starting vortex are connected via the well defined tip vortices at wing tip and the small root vortices at the wing base. At the end of the downstroke, the bound vortex (stopping vortex) shed to the wake and forms a closed elliptical vortex ring (DVS – Downstroke Vortex Structure) behind each wing. The streamwise wavelength of the DVS is λ_{DVS}*=0.22 m=0.57 u/f*. With the end of the downstroke, the upstroke begins and a clockwise rotating starting vortex is generated behind each wing and shed to the wake during the upstroke. Similar to the vortex forming mechanism of the downstroke, the separation of the starting vortex is introduced by the formation and shedding of a vortex sheet. The sheet starts to separate at the wing tip and is fully shed at the end of the upstroke. As with the vortex forming mechanism of the downstroke, the bound and starting vortex are connected via the tip vortices and root vortices. Both vortices changed their rotational direction after passing the lower reversal point. The bound vortex is not completely developed at the wing base while the wing is moving upwards. Therefore, the root vortex and the bound vortex are weak close to the body. At the end of the upstroke, during the anticlockwise wing pitches, the bound vortex (stopping vortex) detaches completely and rolls to the wake, forming an elliptical semi-circled vortex tube (UVS – Upstroke Vortex Structure) behind each wing. The structure of the stopping vortex vanishes quickly as it moves further downstream with a nearly constant flow velocity of *U=3 ms^{-1}*. Heart-shaped vortex loops are generated by a spanwise connection of the vortices of the upstroke and the stopping vortices of

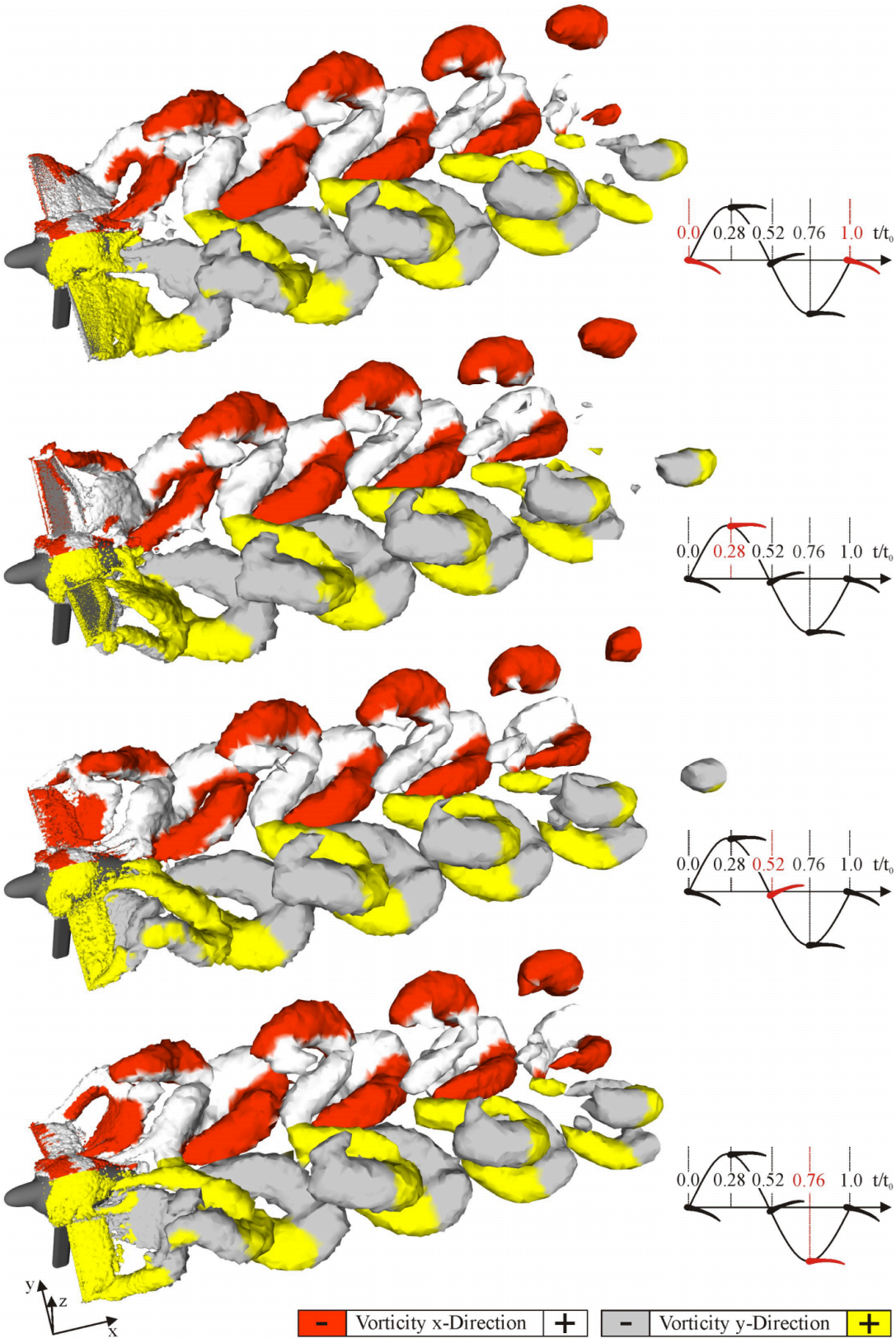

Figure 15: Flow structures superimposed with the vorticty for *k=0.67*.

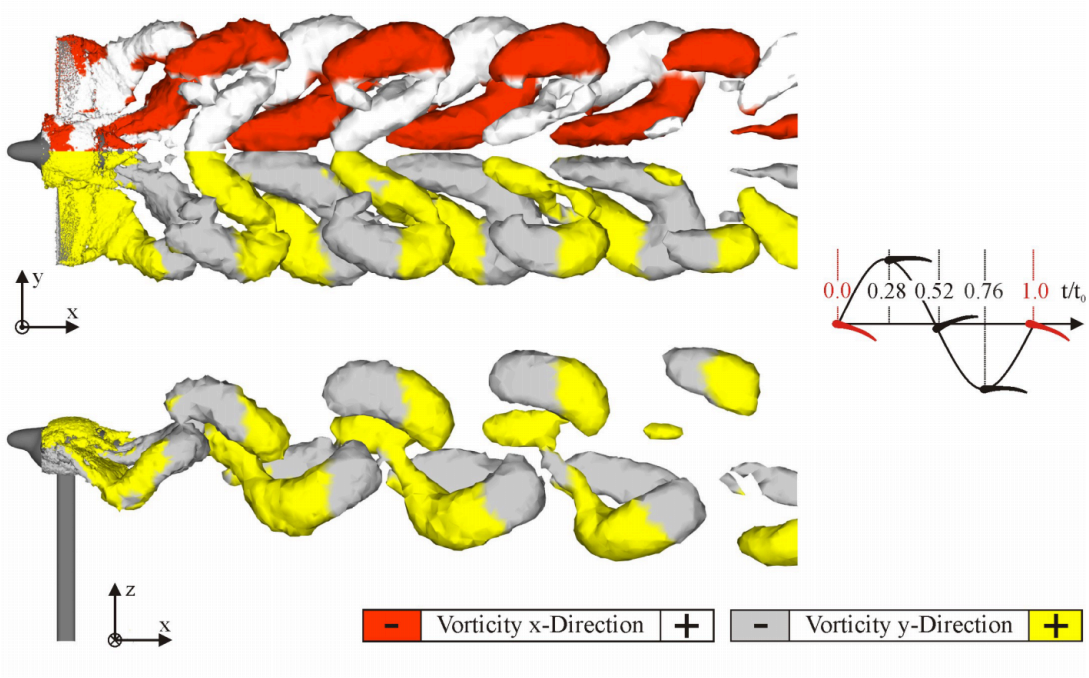

Figure 16: Flow structures superimposed with the vorticty for *k=0.67*.

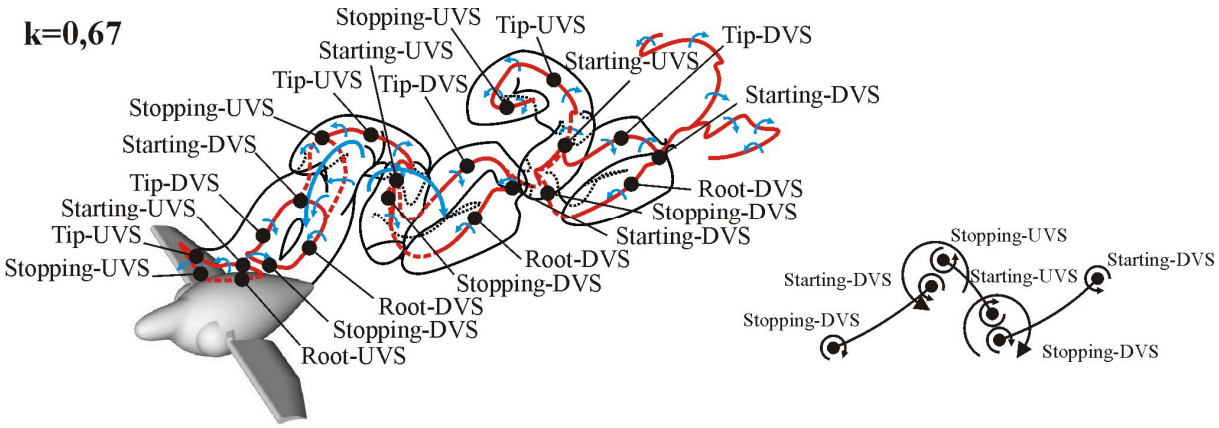

Figure 17: Vortex configuration for *k=0.67*.

the downstroke. The starting vortex of the DVS and the well pronounced tip vortex and the residual structures of the stopping vortex of the UVS are interlocked with each other. The flapping motion causes a traverse alignment of the vortices in the wake while the DVS and UVS are interlocked via their stopping and starting vortices. Because of the synchronously rotating direction of these vortices an opposite momentum exchange occurs at the transition zones and causes a crosswise expansion of the wake. The DVS moves downwards and the UVS moves upwards. Thus, the well defined vortex structures are more exposed to the free stream and the diffusion of the vortex structures is amplified.

k=0.34 (f=8 Hz, U=6 ms^{-1})

At intermediate reduced frequencies (*k=0.34*, *f=8 Hz*, *U=6 ms^{-1}*) the vortex generation mechanism is similar to that of high reduced frequencies during the downstroke but differs during the upstroke. At the beginning of the downstroke, a clockwise rotating bound vortex is produced around each wing. Simultaneously the corresponding anticlockwise rotating starting vortex which is superimposed by anticlockwise and clockwise rotating small scale vortex structures shed to the wake and generate a vortex sheet. The separation starts at the wing tip and shifts to the wing base while moving downwards. At the end of the downstroke the starting vortex is fully separated and the starting, root and tip vortex from a vortex tube behind each wing, whereas the clockwise rotating bound vortex is still attached to the wing and has not been shed. During the upstroke, small scale vortex structures of the bound vortex detach at the outer part of the wing and generate a further vortex sheet which is connected to the well pronounced tip vortex structure. The vortex sheet expands to the wing base and forces the root vortex to decrease. The vortex sheet detaches at the wing tip and remains attached for longer at the inner part of the wing, leading to a partial detachment of the bound vortex (stopping vortex) throughout the upstroke. At the mid wing position, weak oppositely rotating tip and root vortices are developed and shed to the wake. The bound vortex (stopping vortex) and its corresponding vortex sheet are completely detached from the wing at the upper reversal point of the wingbeat cycle. A closed vortex structure (DVS) containing the stopping, starting, tip and root vortices of the downstroke is generated. It is dominated by the large starting and stopping vortices which are merged partially with its corresponding vortex sheets. Because of the flow velocity, streamwise vortex stretching is induced and the DVS is more elliptical. The streamwise wavelength of the DVS is of $\lambda_{DVS} = 0.63\ m = 0.84\ u/f$. The stopping vortices are connected spanwise with each other forming heart-shaped vortex loops. During the wing pitching an anticlockwise rotating starting vortex is generated and the downstroke begins again. An upstroke vortex structure (UVS) is only observed at the end the upward wing motion and is represented by its weak tip and root vortices. Both vortices are connected to the starting vortex of the DVS. While moving downstream with a nearly constant flow velocity of *u=6 ms^{-1}*, the root vortex diffuses quickly, whereas tip vortex is amplified.

k=0.22 (f=8 Hz, U=9 ms^{-1})

At lower reduced frequencies (*k=0.22*, *f=8 Hz*, *U=9 ms^{-1}*) the tip and root vortices dominate the wake pattern. Similar to intermediate reduced frequencies, one closed vortex structure (DVS) per wingbeat cycle is provided by spanwise vortex shedding at the upper reversal point. At the beginning of the downstroke, an anticlockwise rotating starting vortex is shed to the wake. The corresponding vortex sheet of small vortex structures detaching continuously from the upper and lower sides of the wing surface occurs. The vortex sheet starts to separate at the wing tip and is attached for longer to the wing base leading to a continuous and well definded root vortex throughout the downstroke. At the end of the downstroke, the vortex

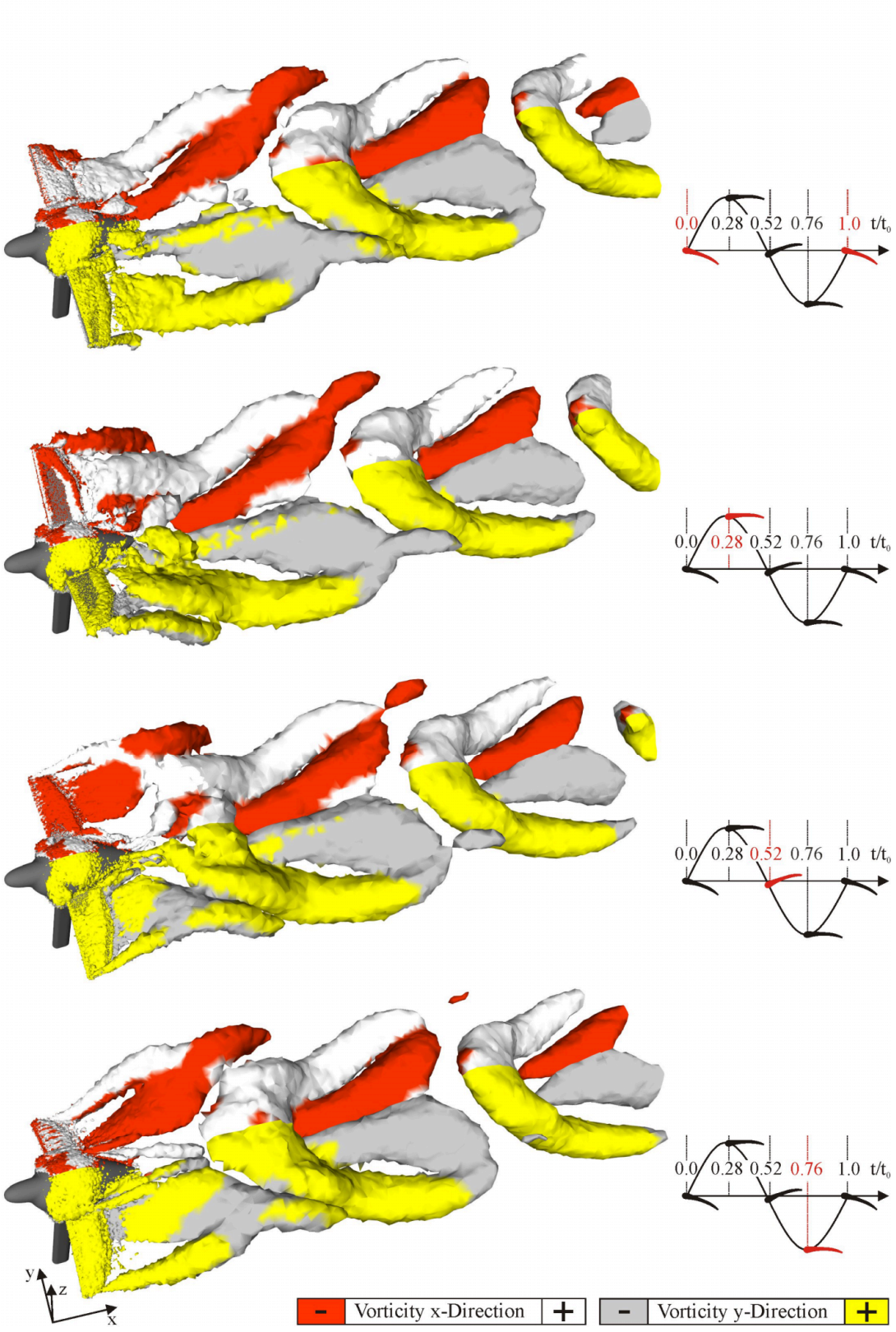

Figure 18: Flow structures superimposed with the vorticty for *k=0.34*.

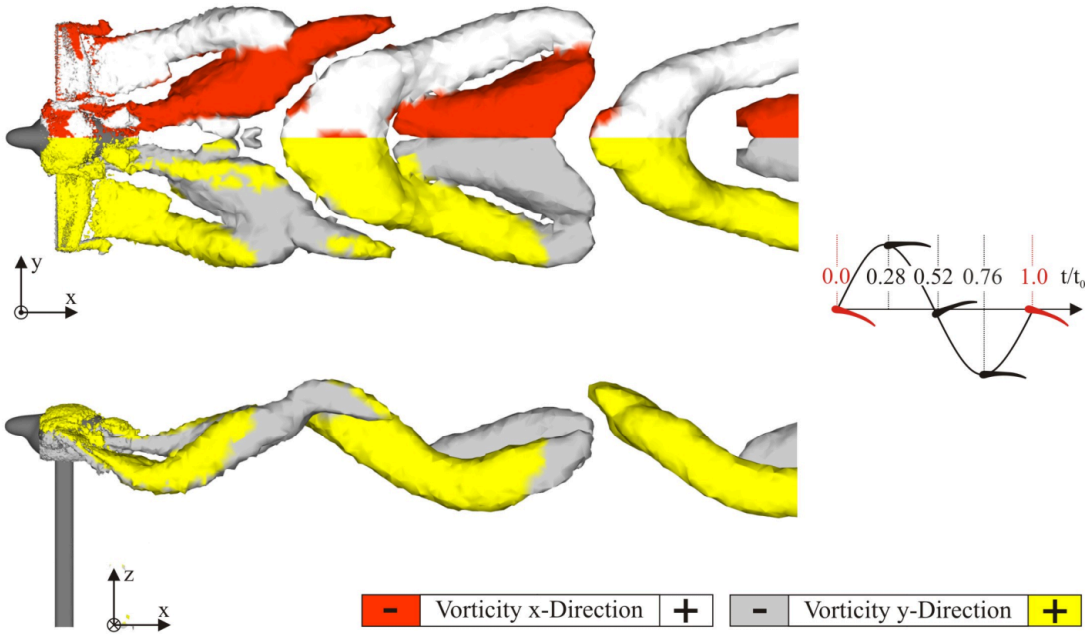

Figure 19: Flow structures superimposed with the vorticty for *k=0.34*.

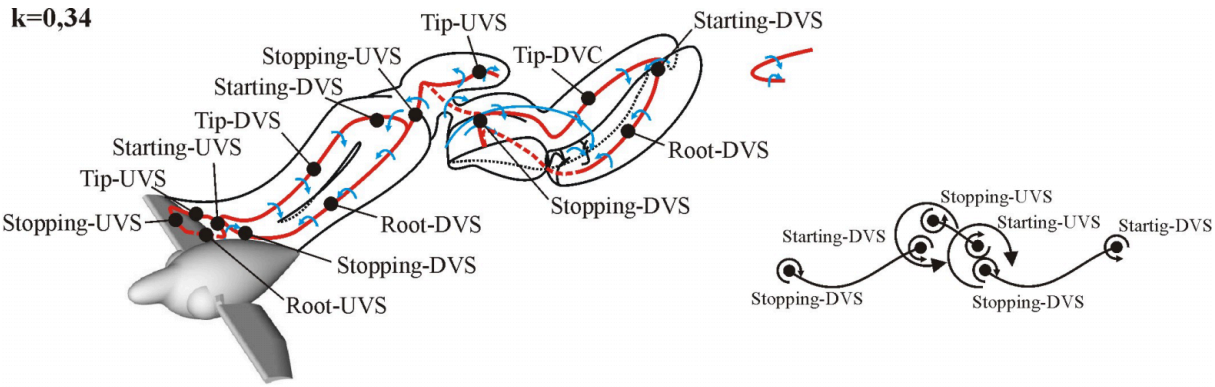

Figure 20: Vortex configuration for *k=0.34*.

sheet is separated and small scale structures related to the bound vortex start to shed at the wing tip. The small scale structures generate a further vortex sheet which extends widely over the wing during the upstroke. It is connected to the tip and root vortices retaining the rotational direction. The root vortex starts to detach from the wing before the upper reversal point of the wingbeat cycle is reached. At the end of the upstroke, the bound vortex (stopping vortex) starts to shed at the outer part of the wing and connects with the already detached root vortex further downstream generating a closed vortex structure (DVS). The anticlockwise

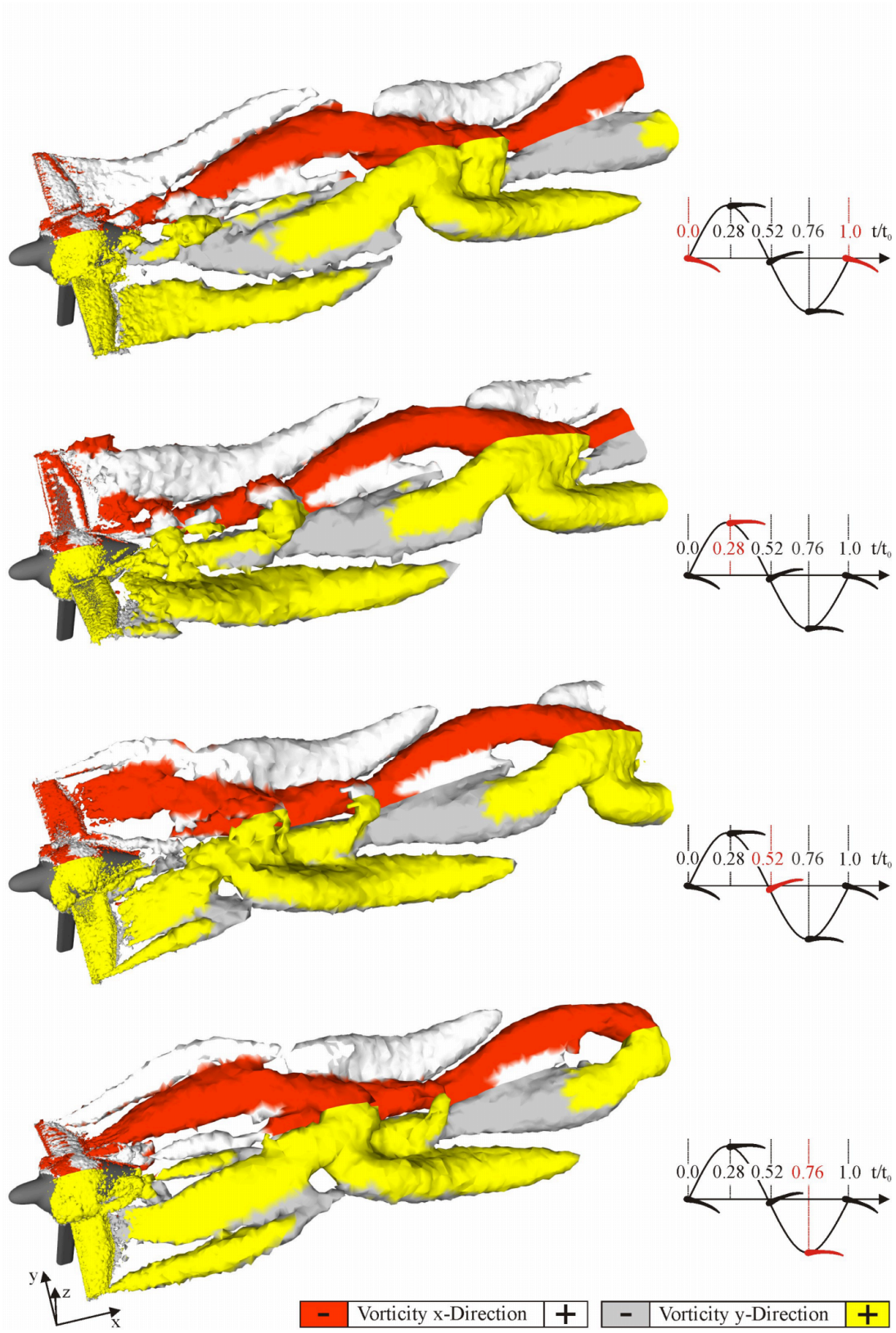

Figure 21: Flow structures superimposed with the vorticty for *k=0.22*.

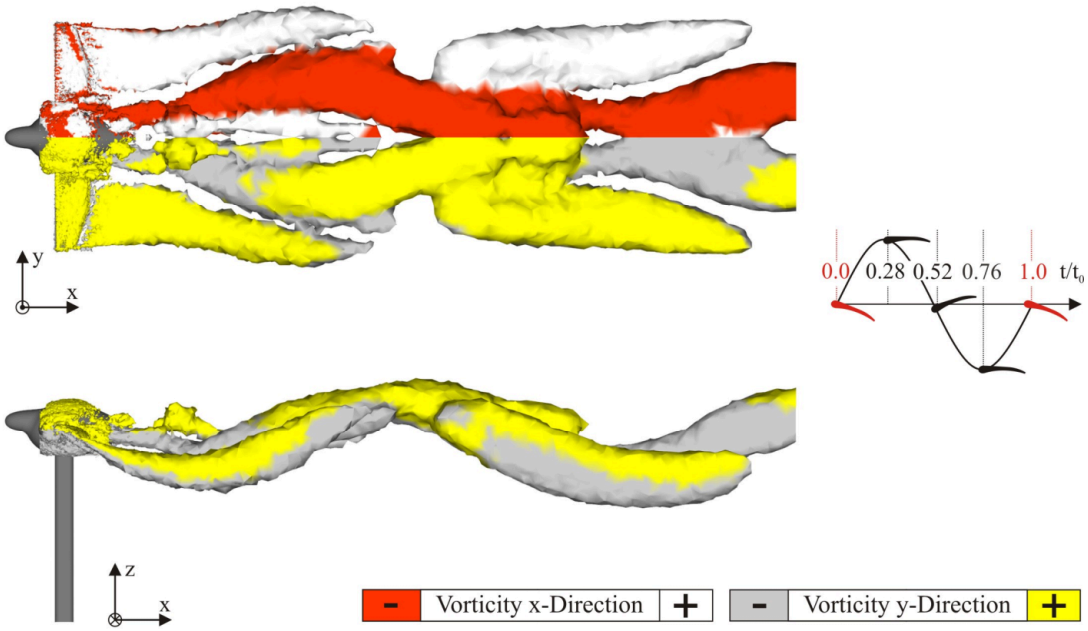

Figure 22: Flow structures superimposed with the vorticty for *k=0.22*.

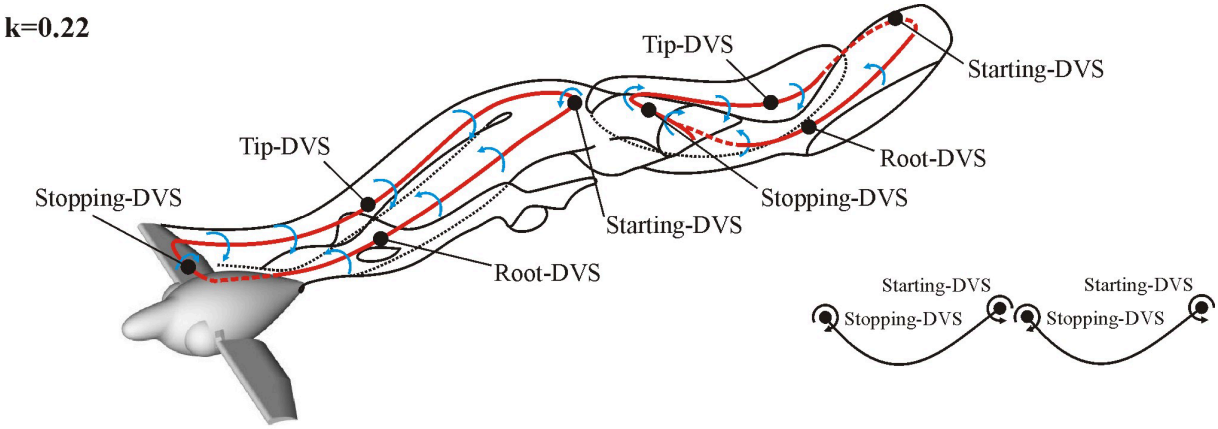

Figure 23: Vortex configuration for *k=0.22*.

rotating starting vortex of the downstroke is shed during the wing pitching. Because the bound vortex remains attached during the upstroke, no upstroke vortex structure (UVS) is produced and the DVS covers nearly the entire wake. The streamwise wavelength of the DVS is of $\lambda_{DVS} = 1.01\ m = 0.896\ u/f$. The omnipresent bound vortex during the wingbeat cycle and the continuous shedding of the corresponding small scale vortex structures lead to a decrease of starting and stopping vortices. Therefore, the wake is dominated by the tip and

root vortices. The stopping vortices are connected spanwise with each other. A crosswise expansion does not occur because the stopping and starting vortices are aligned horizontal and the non-existence of the UVS causes no additional momentum exchange.

5 Conclusion

5.1 Validation

Although, the experimental setup and the numerical approach were of a high degree of complexity, it was possible to obtain comparable results for the validation. The determined velocity profiles and two-dimensional streamline plots show an acceptable agreement for a wide range of flow conditions and physical parameters. The wing motion induced macroscopic vortex structures obtained by the FSI-simulations and the TR-PIV measurements were similar in their temporal and spatial development. Velocity fluctuations and differences of measured and calculated flow fields containing high-frequent, small scale vortex structures can be caused by different factors:

- The high spatial resolution of the TR-PIV measurements resolves a wide spectrum of small scale vortex structures, whereas the coarser spatial resolution of the numerical simulations filters the small scale flow structures and smoothes the flow field.

- For the comparison of the experimental and numerical results, phase-averaging is applied which causes the smoothing of flow quantities. Unfortunately, variations of the periodicity can lead to an increasing and decreasing of the flow velocities.

- Symmetry boundary conditions of the numerical simulations inhibit periodical vortex shedding crosswise behind the KavianFM.

- The wind tunnel geometry and the measurement setup are not provided for the numerical simulation.

Due to quantitative and qualitative results of the experiments and the numerical simulations, it is concluded that the numerical approach is validated in respect to the low frequent and macroscopic flow structures. For an exact simulation of the high-frequent small scale flow and a wide ranging turbulent spectrum a more precise computational approach (Detached Eddy Simulation, Large Eddy Simulation or Direct Numerical Simulation) is required.

5.2 Wake Configuration

For the first time three-dimensional unsteady FSI simulations have been conducted for an avian flight model at a wide range of flapping frequencies and high Reynolds numbers. Although the model does not represent real bird geometry and wingbeat kinematics, flow characteristics that can appear in the aerodynamic performance of birds and bats are described. The present results provide an insight into the complex vortex configurations behind flapping wings helping to understand the three-dimensional and time dependent vortex formation mechanism. At high reduced frequencies ($k=0.67$) the wake differs from the idealized vortex wakes of birds. As a result of the simplified wing motion of the Kavian flight model during the upstroke and its airtight and solid wing design, the upstroke is aerodynamically active leading to a combined shedding of starting and stopping vortices at the reversal points and the well known vortex ring gait (Rayner, 1979a; 1979b; Spedding *et al.,* 1984; Spedding, 1986) was not found. It is assumed that for birds using an inflexible wing motion for the acceleration at medium and fast flight speed, the results show a possible wake model and a similar type of the ladder wake (Pennycuick 1988, Hedrick, et al. 2002). With the increased stroke velocity the circulation of the bound vortices alternates during the upstroke and downstroke leading to an enhanced thrust production whereas the lift is reduced. For decreasing the reduced frequency the bound vortices of the downstroke remain attached to the wing for longer leading to reduction of the upstroke vortex structure whereas the tip and root vortices grow. The transition of the wake configuration forms intermediate vortex structures (Spedding, 1987) which do not belong to one of the two idealized vortex wakes (Rayner and Gordon, 1998). The wake structures are more and more stretched streamwise. For low reduced frequencies the shedding of starting and stopping vortices at the lower reversal point is diffused. The wake structure has been transformd to a double-ringed configuration of the continuous vortex gait (Rayner, 1986, Rayner and Gordon, 1998; Spedding, 1987).

The root vortices close to the body at the wing base lead to closed vortices which are produced behind each wing and has been similar described for slow flying bats (Muijres *et al.,* 2008; Hedenström *et al.,* 2009) and an insect model of a hovering hawkmoth (Van den Berg and Ellington, 1997a; 1997b). The wake configuration of the present results at reduced frequencies of $k=0.34$ seems to be consistent with the wake models of bats (Johansson *et al.*, 2008; Hedenström *et al.,* 2009) for flow velocities around $4\ ms^{-1}$.

The generation of root vortex structures has been verified for bats and insect models and a basic question concerning root vortex structures arises: Do root vortices occur during flapping flight of birds? Considering the present results and those for bats and insect models, the formation of a single vortex ring configuration requires a wing motion synchronized circulation around the body to ensure the consistent spanwise circulation of the shed vortices. Otherwise, the vortex formation

across the wingspan can be interrupted and weak root vortices are shed and can lead to the generation of closed vortex rings behind each wing. This is not clearly verified for flying birds until now. Further numerical and experimental studies are required using numerical representation of a real bird wing for numerical simulations to bridge the gap between the different types of wake models.

5.3 Further Model Developments

The numerical flow simulation of a real bird model is ongoing research at the Institute of Fluid Mechancis at the Karlsruhe Institute of Technology, Germany. By means of wind tunnel test with living flycatchers at the Department of Theoretical Ecology, Lund University, high speed videos of flapping flight were recorded. Applying the stereographical software PHOTOMODLER, the exact wing geometry can be extracted at different time steps throughout the wingbeat cycle. Therefore three-dimensional models of different wing positions at different time steps were developed, see Fig. 24. For a numerical simulation of the wing motion, a smoothing algorithm (Perschall et al., 2007) was applied to the different the model interpolating between the wing positions.

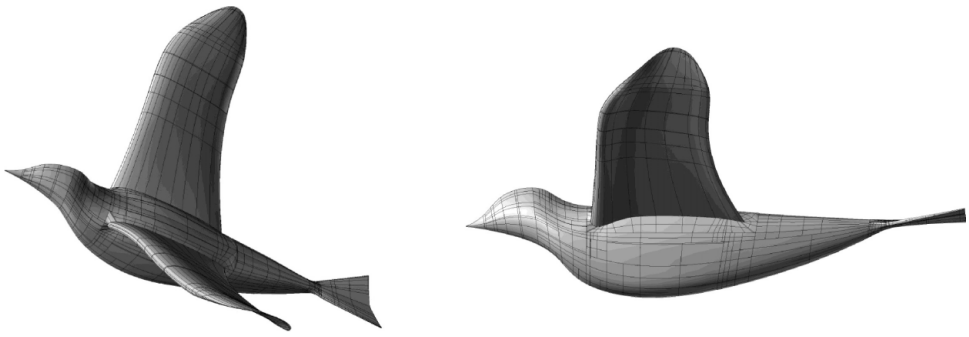

Figure 24: Numerical flow model of a flycatcher with simplified body

Furthermore a structural model taking the material properties and a simplified composite of the bird wing into account will be used for the FSI simulations. Fig. 25 shows the simplified wing model. The bird wing is subdivided into different components with varying material properties. It consists of frames, membranes and tubes. The wing bones are modelled by cylindrical tubes and hinges (Fig 25, 4). The primary and secondary feathers are represented by frames (Fig 25, 1) and membranes which are tighten between the frames (Fig 25, 2). The converts are modelled by overlapping membranes (Fig 25, 3). The corresponding material parameters result from literature, tension and bending tests, see Chapter 1.1. As with the material properties of the feather shaft, the Young's Modulus of the frames increases from $E = 2.5\ GPa$ (wing base) to $E = 4.0\ GPa$ (wing tip). The Young's Modulus of the membranes varies between $E=10.0\ MPa$ and $E=2.0\ GPa$. The

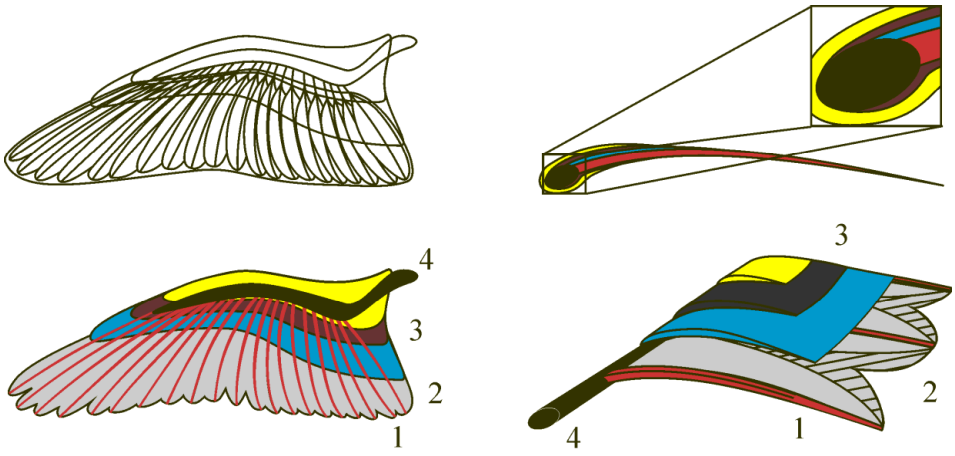

Figure 25: Structural model of the bird wing. 1: feather shafts, 2: membranes between the feather shafts, 3: coverts, 4: wing bone structures

air-permeability of the bird feathers are modelled by porosities which vary throughout the wingbeat motion.

The implementation, generation and numerical simulation of the flow model, structural model and the interaction of both models is part of ongoing research of the unsteady aerodynamics of the avian flight.

A References

Azuma, A., (2006). The Biokinetics of Flying and Swimming. 2nd Edition. AIAA Education Series

Bonser, R., Purslow. (1995). The young's modulus of feather keratin. J. Exp. Biol. 198, 1029-1033.

Dickinson, M. H., Götz, K.G. (1993). Unsteady aerodynamic performance of model wings at low Reynolds numbers. J. Exp. Biol. 174, 45-64.

Ellington, C., Van den Berg, C., Willmott, A., Thomas, A. (1996). Leading edge vortices in insect flight. Nature, 384, 626-630.

Fluent 6.3 User Guide. (2006). Fluent

Hedenström, A. (2006). Vortex wakes generate by robins Erithacus rubecula during free flight in a wind tunnel. J. R. Soc. Interface. 3, No. 7, 263-276.

Hedenström, A., van Griethuijsen, L., Rosén, M., Spedding, G.R. (2006). Vortex wakes of birds: recent developments using digital particle image velocimetry in a wind tunnel. Animal Biology. 56, 4, 535-549.

Hedenström, A., Johansson, L.C., Wolf, M., Von Busse, R., Winter, Y., Speeding, G.R. (2007). Bat Flight Generates Complex Aerodynamic Tracks. Science. 316, 894-897.

Henningsson, P., Spedding, G. R., Hedenström, A. (2008). Vortex wake and flight kinematics of a swift in cruising flight in a wind tunnel. J. Exp. Biol. 211, 717-730.

Hedenström, A., Johansson, L. C., Wolf, M., von Busse, R., Winter, Y., Spedding, G. R. (2009). Science. 316, 894-897

Hedrick, T., Tobalske B., Biewener, A. (2002). Estimates of circulation and gait change based on three-dimensional kinematic analysis of flight in cockatiels (nymphicus hollandicus) and ringed turtle-doves (streptropelia risoria). J. Exp. Biol. 205, 1389-1409.

Hoffmann, R. (2005). Grundlagen der Frequenzanalyse, Expert verlag, Renningen, 2. ed.

Hubel, T.Y., Hristov, N., Swartz, S. and Breuer, K. (2009). Time-resolved wake structure and kinematics of bat flight. Exp.Fluids. 46, 933-943.

Hubel, T., Tropea, C. (2005). Wirbelbildung hinter schlagenden Tragflächen. Bionik. ISBN: 978-3-540-21890-6; 51-61. Springer

Jeong, J., Hussain, F. (1993). On the identification of a vortex. J. Fluid Mech. 285, 69-94.

Johansson, L. C., Wolf, M., von Busse, R., Winter, Y., Spedding, G. R., Hedenström, A. (2008). The near and far wake of Pallas' long tongued bat (Glossophaga soricina). J. Exp. Bio. 211, 2909-2918.

Kokshaysky, N. V. (1979). Tracing the wake of a flying bird. Nature. 279, 146-148.

Launder, B.E, Spalding, D.B. (1972). Lectures in Mathematical Models of Turbulence. Academic Press, London, England.

Menter, F. R. (1993). Zonal Two Equation k-w Turbulence Models for Aerodynamic Flows. AIAA Paper. 93-2906.

Menter F.R., (1994). Two-Equation Eddy-Viscosity Turbulence Models for Engineering Applications. AIAA Journal. 32, 8, 1598-1605.

Menter, F.R. Kuntz, M., Langtry, R. (2003). Ten Years of Industrial Experience with the SST Turbulence Model. Turbulence, Heat and Mass Transfer 4, ed: K. Hanjalic, Y. Nagano, and M. Tummers. Begell House, Inc. 625 - 632.

Murijes, F.T., Johannson, L. C., Barfield, R., Wolf, M., Spedding, G. R., Hedenström, A. (2008). Leading-Edge Vortex improves Lift in slow-flying Bats. Science. 319, 1250-1253.

Oertel, H. jr., Ruck, S. (2011). Bioströmungsmechanik. Vieweg-Teubner Verlag.

Oertel, H. jr. (2009). L. Prandlt, Essentials of Fluid Mechanics. 3rd Edition. Springer Verlag.

Park, K.J., Rosén, M., Hedenström, A. (2001). Flight kinematics of the barn swallow Hirundo rustica over a wide range of speeds in a wind tunnel. J. Exp. Biol. 204, 2741-2750.

Pennycuick, C.J. (1988). On the reconstruction of pterosaurs and their manner of flight, with notes on the vortex wakes. Biol. Rev. 63, 299-331.

Perschall, M., Spiess, M., Schenkel, T., Oertel, H. jr. (2007). Code adapter for arbitrary prescribed motion and deformation using fluent and mpcci. In: MpCCI 8th User Forum, 126-131.

Poelma, C., Dickson, W. B., Dickinson, M. H. (2006). Time-resolved reconstruction of full velocity field around a dynamically scaled flapping wing. Exp. Fluids. 41, 213-225.

Purslow, P., Vincent, J. (1978). Mechanical properties of primary feathers from the pigeon. J. Exp. Biol. 72, 251-260.

Raffel, M., Willert, C., Kompenhans, J. (2007). Particle Image Velocimetry–a practical guide. Springer, 2. ed.

Rayner, J. M. V. (1979a). A vortex theory of animal flight. I. The vortex wake of a hovering anima. J. Fluid Mech. 91, 697-730.

Rayner, J. M. V. (1979b). A vortex theory of animal flight. II. The forward flight of birds. J. Fluid Mech. 91, 731-763.

Rayner, J. M. V. (1986). Vertebrate flapping flight mechanics and aerodynamics, and the evolution of flight in bats; Biona Report 5; 27-74. Stuttgart: Gustav Fischer Verlag

Rayner, J. M. V., Gordon, R. (1998). Visualization and modelling of the wakes of flying birds. In Biona Report. 13, 165-173. Jena: Gustav Fischer Verlag.

Roache, P. J. (1998). Verification and Validation in Computational Science and Engineering, Hermosa Publishers, Albuquerque, NM.

Rosén, M., Spedding, G.R., Hedenström, A. (2004). The Relationship between wingbeat kinematics and vortex wake of a thrush nightingale. J. Exp. Biol. 207, 4255-4268.

Ruck, S., Oertel, H. jr. (2010). FSI Simulation of an avian flight model. J. Exp. Biol. 213, 4180-4192

Ruck, S., Tischmacher, M. (2010). Numerical and experimental investigation of the unsteady aerodynamics behind flapping wings using FSI and PIV. Proceedings of the 18th Conference on Laser Methods in Flow Measuring Technique, 19.1-19.9.

Ruck, S., Tischmacher, M., **Schenkel, T., Oertel H. jr**. (2010). Biofluidmechanics of Avian Flight: Recent Numerical and Experimental Investigations. WCB - IFMBE Proceedings 31, Singapore, pp. 14-17, 2010.

Ruck, S., Schenkel, T., Oertel H. jr. (2010). Vortex Configuration Behind Flapping Wings. Proceedings IUTAM Symposium on Bluff Body Wakes 2010, Capri, Italy, pp 229 – 232,

Spedding, G. R., Rayner, J. M. V., Pennycuick, C. J. (1984). Momentum and energy in the wake of a pigeon (Columba livia) in slow flight. J Exp. Biol. 111, 81-102.

Spedding, G. R., (1986).The wake of a jackdaw (Corvus monedula) in slow flight. J. Exp. Biol. 125, 287-307.

Spedding, G. R. (1987). The wake of a kestrel (Falco tinnunculus) in flapping flight. J. Exp. Biol. 127, 59-78.

Speeding, G. R., Rosén, M., Hedenström; A. (2003). A family of vortex wakes generated by a thrush nightingale in free flight in a wind tunnel over its entire natural range of flight speeds. J. Exp. Biol. 206, 2313-2344.

Tian, X., Iriarte-Diaz, J., Middelton, K., Galvao, R., Israeli, E., Roemer, A., Sullivan, A., Song, A., Swartz, S., Breuer, K. (2006). Direct measurements of the kinematics and dynamics of bat flight. Bioinsp. Biomim. **1**, S10-S18

Tobalske, B.W. (2000). Biomechanics and Physiology of Gait Selection in Flying Birds. Physiological and Biomechanical Zoology. 73, 6, 736-750.

Tobalske, B.W. (2007). Biomechanics of bird flight. J. Exp. Biol. 210, 3135-3146.

Tobalske, B.W., Hedrick, T.L., Biewener A.A. (2003). Wing kinematics of avian flight across speeds. J. Avian Biology. 34, 177-184.

Tobalske, B.W. Dial, K.P. (1996). Flight kinematics of black-billed magpies and pigeons over a wide range of speeds. J. Exp. Biol. 199, 263-280.

Van den Berg, C., Ellington, C. P. (1997a). The vortex wake of a `hovering' model hawkmoth. Phil. Trans. R. Soc. Lond. B 352, 317-328.

Van den Berg, C., Ellington, C. P. (1997b). The three dimensional leading-edge vortex of a `hovering' model hawkmoth; Phil. Trans. R. Soc. Lond. B 352, 329-340.

Videler J.J., Stamhuis E.J., David G., Povel E. (2004). Leading-Edge Vortex Lifts Swifts. Science. 306, 1960-1962.

Wilcox, D.C. (1988). Reassessment of the Scale Determining Equation for Advanced Turbulence Models. AIAA Journal. 26, 11, 1299-1310.

Willmott, A., Ellington, C., Thomas, A. (1997) Flow visualization and unsteady aerodynamics in the flight of the hawkmoth. Phil. Trans. 352, 303-316.

ISBN 978-3-86644-761-5